Interfacial Stability of Perovskite Solar Cell Layers

A THESIS SUBMITTED TO THE FACULTY OF THE UNIVERSITY OF MINNESOTA BY

Eleanor R. K. Sternberg

IN PARTIAL FULFILLMENT OF THE REQUIREMENTS FOR THE DEGREE OF MASTER OF SCIENCE APPLIED MATERIAL SCIENCE

Dr. Zhihua Xu

May 2025

Acknowledgements
Major thanks are extended to Dr. Zhihua Xu, without whom this project would not have been possible, committee members Dr. Sam Toan and Dr. Paul Kiprof for serving on my committee, and to Dr. Michael Pluimer for providing the laboratory space where this work was conducted. Big thanks to all three DGS Applied Material Science who have served during my time at UMD, my AMS cohort and office-sharers in Chemical Engineering, without whom graduate school would have been a great deal more dull.
Thanks also to my friends and family, for hearing me out as I put the pieces of this project together, and for their enduring love and support.

Abstract

Organometal halide (OMH) perovskites are chemically unstable when exposed to oxygen, heat, and moisture. The long term stability of organometal halide perovskite solar cells (PSCs) may be enhanced by understanding two interactions. The first is between the perovskite and the electron transport layer (ETL). The second is between the perovskite and the hole transport layer (HTL). It has been reported that the ionic defects in the perovskite layer (for example, iodine ions) may drift to and accumulate at the interfacial areas of the ETL and the HTL over time, leading to extensive chemical degradation of PSCs. In this project, we adopt ultraviolet-visible (UV-Vis) absorption and steady-state photoluminescence (PL) emission spectra to investigate the degradation processes of two OMH perovskites, methylammonium lead iodide ($MAPbI_3$), and methylammonium lead bromide ($MAPbBr_3$) with the aim to understand the exact effects of ion migration and accumulation at ETL and HTL on long term stability of perovskites. Our research reveals that the interaction of the migrated ions with TiO_2 ETL significantly accelerates the degradation of both OMH perovskites, while the interfacial interactions at spiro-OMeTAD (2,2',7,7'-Tetrakis[N,N-di(4-methoxyphenyl)amino]-9,9'-spirobifluorene) HTL yield lesser effect on the stability of perovskites. The results also suggest ion accumulation at the ETL/HTL affects the interfacial charge transfer processes.

List of Figures

Chapter 1: Introduction

Interest in perovskite materials has waxed and waned since their discovery in 1839. At the time, the first perovskite discovered, calcium titanate ($CaTiO_3$), was of interest to geologists as a unique mineral. In the modern era, it can be reduced to provide titanium metal[1]. In the last approximately fifteen years, interest in using perovskites as photovoltaic materials in solar cells has increased significantly. The first paper to demonstrate that organometal halide (OMH) perovskites were capable of converting visible light to electricity came from Miyasaka et al., in 2009. In Miyasaka, methylammonium lead iodide ($MAPbI_3$), and methylammonium lead bromide ($MAPbBr_3$) are realized for the first time as "visible-light sensitizers" capable of converting light into power, when organized on mesoporous TiO_2. The photoelectrochemical cell Miyasaka and colleagues built, using $MAPbI_3$, had an efficiency of 3.8%[2]. However, it was not until 2012 that enough was known about the structure-property relationship to cause the proliferation of research and published papers known to the field today. In 2012, researchers discovered that the perovskite material would maintain its integrity in contact with a solid state hole transporter, spiro-OMeTAD (2,2',7,7'-Tetrakis[N,N-di(4-methoxyphenyl)amino]-9,9'-spirobifluorene), making a solid-state photovoltaic cell possible and increasing device efficiencies up to nearly 10%[3]. As of March 2025, perovskite solar cells (PSCs) have a record certified efficiency of 27%[4]. Research into further device optimization continues, especially with respect to stability and manufacturing.

1.1 Perovskite Solar Cells

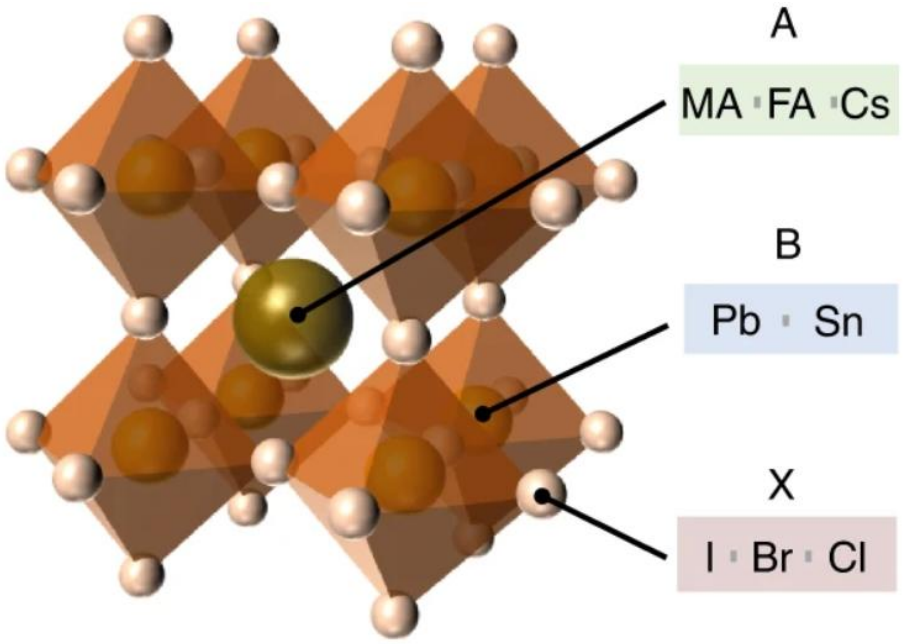

Figure 1: Diagram of the crystal structure of ABX_3 perovskites. {1}

The key material in PSCs are the organometal halide perovskites which serve as light absorbers. The OMH perovskites have ABX_3 structure, where "A" is an organic (methylammonium (MA) or formamidinium (FA)) cation, B is a metal (Pb, Sn, Bi) ion, and X is a halide (I, Br, Cl), as shown in Figure 1. The "B" group sits inside an octahedron that is formed with six halides, and the "X" group is located at the vertices. The "A" group rests between the repeating octahedral unit. Perovskites can take on other crystal conformations as well; the most common other structures are orthorhombic and cubic[5].

OMH perovskites are direct bandgap semiconductors[6], and so they have high light absorption coefficient, making them ideal for solar applications. Compared to indirect bandgap semiconductors, direct bandgap semiconductors are desirable because they can absorb a greater

number of photons with the same film thickness, increasing the efficiency of the overall photovoltaic cell. Other promising properties include that the high efficiency with which perovskite can convert sunlight into electricity, that perovskites have good electron and hole mobility, that perovskite materials are relatively inexpensive compared to production costs for silicon solar cells, and that perovskites have tunable bandgaps to further their efficiency. OMH PSCs are an appealing alternative to traditional silicon solar cells because they can be solution processed into thin films (via processes like spin coating) at much lower temperatures[7] than silicon wafers need to be processed at. In the Czochralski method of making silicon wafers, processing temperatures are typically above 1400℃, which becomes expensive when it is part of a long-term or continuous manufacturing process[8].

Iodine is the most common halide used in PSCs because of its small bandgap. Bromide perovskites are popular for their improved chemical stability, although their bandgap is somewhat wider than their iodine counterparts. Lead is a very common metal in ABX_3 perovskite materials for solar applications. While lead-based perovskites boast impressive power conversion efficiencies, the toxicity of lead to both humans and the environment pose complications when considering fabrication and installation of a PSC[9]. Other metals considered for a role in organometal halide perovskites for photovoltaic applications include tin (Sn) and bismuth (Bi). Sn-based PSC efficiencies lag behind those of Pb-based PSCs by approximately 10-15%[10]. Sn also has a low redox potential in the ambient atmosphere, which means that Sn^{2+} will rapidly convert to Sn^{4+}, destroying the perovskite crystal structure and any hope of converting light into power. Sn-based PSCs fabricated with organic “A” group cations like MA or FA are more sensitive to heat and moisture than their Pb-based counterparts. Sn^{2+} carries

additional health warnings for human beings, for its ability to displace other divalent elements in the body such as Zn, Cu, and Ca[11]. Bismuth-based PSCs suffer from their raw materials being considerably more expensive to obtain, and lower PCEs than Sn-based PSCs[12].

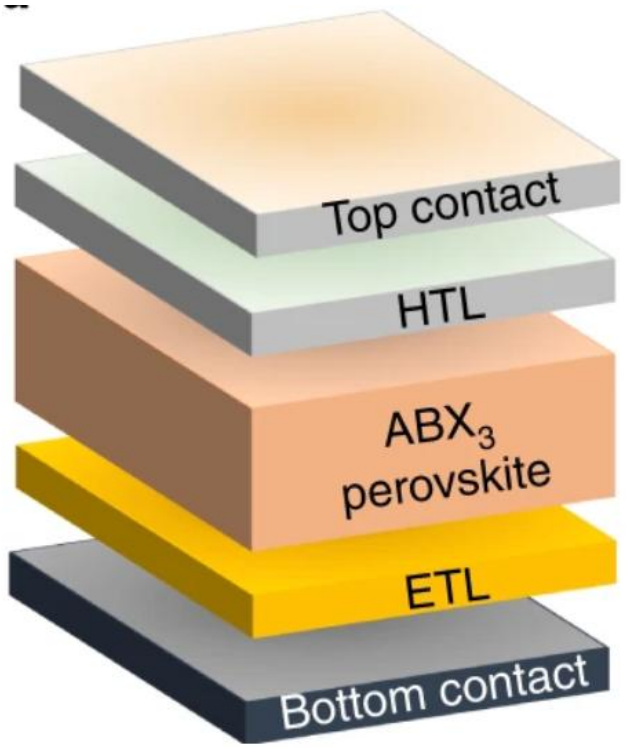

Figure 2: Device architecture of a perovskite solar cell.{1}

A typical device configuration for PSCs is shown in Figure 2, where the organometal halide perovskite, for example $MAPbI_3$, is sandwiched by an electron transporting layer (ETL) and a hole transporting layer (HTL), which are in direct contact with a cathode (for example, fluorine-doped indium oxide (FTO)) and an anode (for example, Au or Ag), respectively. When a PSC is exposed to light, electron and hole pairs are generated in the perovskite layer. Then the electrons flow to ETL and are collected by the cathode, while the holes flow to HTL and are collected by the anode.

In order for those electrons to flow between different materials, there is another material property to consider. A band gap is the space between energy levels in a material, as shown in figure 3. Below the band gap is the valence band, where electrons are involved in the bonds that hold atoms together. Above the band gap is the conduction band, which are the lowest energy empty atomic orbitals. When electrons are energized up to the conduction band by heat or light, the material can conduct electricity. Semiconductors all have slightly different band gaps, depending on what they're made of. When different materials are joined together to conduct electricity, the sites where their conduction and valence bands meet is called a heterojunction. Materials in semiconductors are often carefully chosen for their "band gap alignment", or careful positioning of the edges of heterojunctions to ensure a steady flow of electrons.

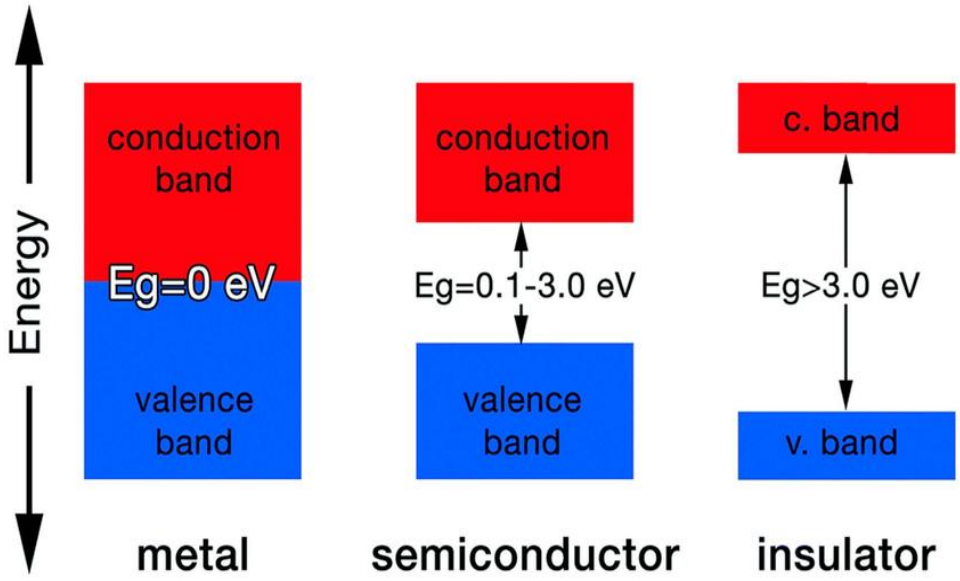

Figure 3: Band gap diagram of metals, semiconductors, and insulators. {2}

As shown in Figure 4, when incident photons enter at the perovskite layer, and those with sufficient energy excite an electron into the conduction band, and an oppositely charged hole

stays in the valence band. They move in opposite directions; the electron moves towards the ETL, and the hole moves towards the HTL. The HTL/Perovskite/ETL system is carefully chosen for its band gap alignment, and so the photogenerated electrons and holes are separated and transported efficiently. If the electrons or holes reach the cathode and anode, they can be sent to either a device that requires power, or a storage device like a battery. During the transporting processes, electrons and holes need to avoid the defects in the crystal which cause charge recombination. Similarly, poor alignment where the perovskite material meets the HTL and ETL can also cause recombination.

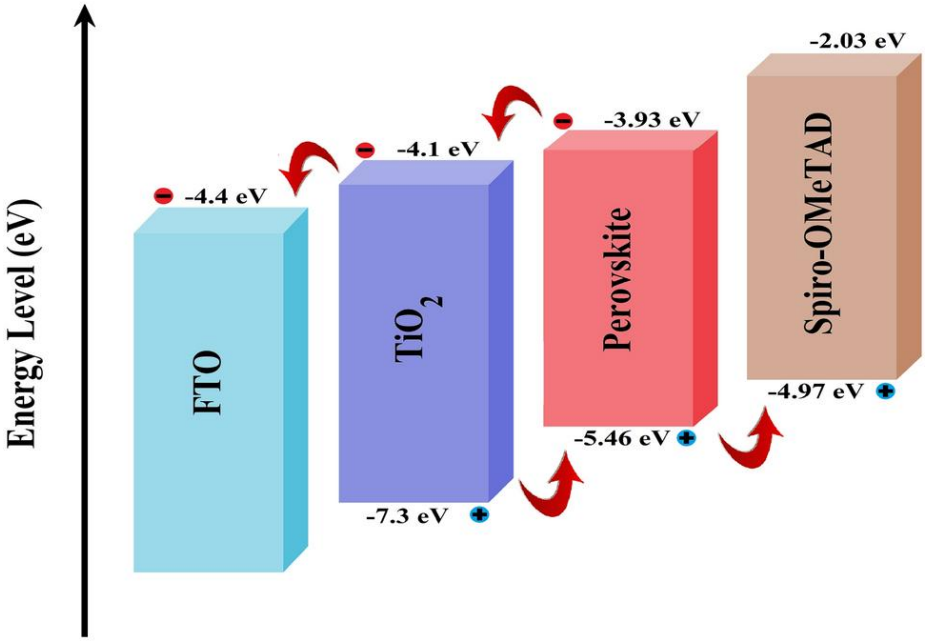

Figure 4: Band gap alignment of layers within a perovskite solar cell. {3}

Spiro-OMeTAD (2,2',7,7'-Tetrakis[N,N-di(4-methoxyphenyl)amino]-9,9'-spirobifluorene) is a common and inexpensive HTL material used in the fabrication of PSC devices. It is popular for the stability of its morphology, ease of solution processability, and good electronic properties. Spiro-OMeTAD is not without its drawbacks, however. Post processing

migration of iodine atoms between the perovskite and spiro-OMeTAD can accelerate degradation[13]. Other drawbacks include low hole conductivity[14], and chemical sensitivity to illumination, humidity, and temperature[15]. Many different species of dopants are being explored as ways to improve the stability and hole mobility of spiro-OMeTAD. P-type dopants like FK209 and *t*-BP are being explored for their ability to improve hole mobility[14] and dopants like ferrocene, $Zn(TFSI)_2$, and TBA-TFSI are being explored for their contributions to overall device stability[15].

Titanium dioxide (TiO_2) is a popular and inexpensive ETL material commonly used in the study and fabrication of PSCs. TiO_2 has several qualities that make it an ideal ETL. TiO_2 is chemically stable, and doesn't degrade in the presence of moisture, heat, and ultraviolet radiation. TiO_2's mesoporous structure increases the overall interfacial contact area with the perovskite material, allowing for greater charge extraction and decreased recombination. TiO_2 is less environmentally harmful than other ETL materials like SnO_2, which also makes it easier to incorporate into a large-scale manufacturing process. Finally, TiO_2 has easily tunable morphology (brookite, rutile, anatase) that affect changes in its bandgap. This makes TiO_2 accessible to multiple types of perovskites and devices. Electrons that travel through TiO_2 as an ETL may do so either by continuous travel (provided the electron has sufficient energy) or by quantum tunneling[16]. As far as its weaknesses, TiO_2 has a lower electron mobility than top-performing materials like graphene and controlling for surface defects when depositing TiO_2 is difficult. These factors lead to increased recombination. Dopant materials like Sn and Ga are being explored as possible ways to increase the electron mobility and decrease the incidence of crystalline defects[17, 18].

1.2 Degradation of Perovskites

Stability of the OMH perovskites (the ability to resist degradation) is one of the greatest challenges in commercializing PSC technology. Because silicon solar cells are stable at much longer timescales (up to 25 years), perovskites must compete on similar timescales. However, perovskites are vulnerable to chemical degradation by several different methods: exposure to moisture, oxygen, and heat; voids in the crystal structure including evaporation of methylammonium; and instability from ion migration. One of the primary driving factors behind this instability is that ions diffuse throughout the crystal structure, which creates both voids and interstitials, leading to instability in the crystal structure over time. Research demonstrates several strategies that contribute to improves PSC stability, including tuning the "A" group to prevent the perovskite crystal from shifting between octahedral and orthorhombic configurations, and providing sufficient encapsulation so that water and oxygen gas ambient in the atmosphere do not react with the perovskite material[19].

Methylammonium lead iodide ($MAPbI_3$) has been the most widely researched perovskite for solar cell applications. However, this iodide perovskite is sensitive to many environmental factors like temperature, ultraviolet light, and humidity. It has access to both reversible and non-reversible decomposition pathways as shown in McGovern:

$$\text{Reversible: } CH_3NH_3PbX_3(s) \rightleftharpoons CH_3NH_2(g) + HX(g) + PbX_2(s) \quad (1)$$

$$\text{Non-reversible: } CH_3NH_3PbX_3(s) \rightharpoonup NH_3(g) + CH_3X(g) + PbX_2(s) \quad (2)$$

Research has also noted that the bromide perovskite, $MAPbBr_3$, has a few key distinctions. It only experiences the reversible decomposition pathway noted in equation 1 above. $MAPbBr_3$ has a higher vacancy formation energy, which decreases instances of halide ions migrating in the crystal lattice. The bromide perovskite also sterically inhibits MA^+ migration

due to having a smaller lattice because of the shorter length and greater strength of the Pb-Br bond[20].

There is a large body of literature dedicated to strategies for increasing the stability of perovskite materials. Some studies look at combining additives with the perovskite. For example, researchers studied the addition of Lewis base molecules to form favorable crystals and bond with Pb at the grain boundary to stabilize the crystal, decrease the number of defects and inhibit ion migration[21]. Other stability studies interrogate spin-coating or other processes involved in the making of perovskite materials. In one such paper, Fie et al. spin-coated a thiourea precursor and ethyl acetate anti-solvent onto their substrate. This treatment slows the rate at which MAPbI3 crystallizes on the substrate. The resulting larger grain size increases charge transport within the perovskite material[22]. Other times, stability studies focus on the PSC device. Two dimensional materials like transition metal disulfides, graphene, black phosphorus quantum dots, and metal-organic frameworks have become of interest for use as HTl, ETL, or electrodes in PSC devices[23].

It is worth noting that OMH perovskite materials are mixed ionic-electronic conducting materials. Ions of all species, and the defects they leave behind, diffuse through the material, driven by light or an electrical field. These ions will only reach beyond the HTL or ETL when under significant stress, such as an applied voltage or illumination. Where an electrical or thermal gradient is present in the crystal, ions may become permanently bound at interfaces to the HTL or ETL, reducing the efficiency of the PSC because the halide ions no longer occupy their place in the conducting lattice. There is research that has pointed out that the ion migration and interaction with the interfaces might affect the long-term stability of perovskite solar cells

1.3 This Project

Most research on perovskite stability has focused on either the perovskite itself, or on the PSC as a device. This project focuses on the interfacial chemistry within a PSC device, and aims to determine whether or not the interfaces are contributing to degradation.

In this project, we use spiro-OMeTAD as the hole transporting layer (HTL), methylammonium lead iodide and methylammonium lead bromide ($MAPbI_3$ and $MAPbBr_3$) as the perovskite layers, and titanium dioxide (TiO_2) as the electron transporting layer (ETL). To explore the interfaces, samples of just the perovskite were prepared to understand its behavior in the experimental conditions. Additionally, samples of the HTL/Perovskite and Perovskite/ETL were prepared, to isolate those interfaces specifically, and a sample of all three layers, HTL/Perovskite/ETL, to explore the interfaces as they would exist in a PSC. This project also explored interactions with a second perovskite, $MAPbBr_3$.

For this project, building solid state layers of each component by spin-coating on top of a clear glass substrate would achieve four integral objectives. First, it would reduce costs because the lab wouldn't have to purchase additional materials needed for building full solar cells. Second, it would reduce the time needed to complete the project. Because a master's degree is typically two years long, and it can take two to three years to master building functional solar cells, this was unlikely to produce quality results with the time available. Third, it would reduce the chemical complexity of the system as we measured it, ensuring that what we observed was interaction within the HTL/Perovskite/ETL system and not a chemical reaction with, for example, housing, a dopant, or an electrical contact. Fourth, the clear glass substrate would create ease of measurement for PL and UV-Vis spectroscopy.

UV-Vis absorption spectroscopy was used to monitor the degradation processes of perovskite samples, under the supposition that the change of absorption of the semiconductor thin films indicates the degree of the degradation. Semiconductor materials absorb light where the photon has energy greater than or equal to the bandgap energy. Absorbing light creates a broad peak on the recorded spectrum. The absorption (absorbance) of the semiconductor is calculated by the equation (3) for absorbance:

$$A = -\log_{10}(I/I_0) \quad (3)$$

Where I is the transmitted light intensity, and I_0 is the incident light intensity.
The edge of the absorbance peak corresponds to the bandgap via the Tauc equation (4):

$$(\alpha h\boldsymbol{\nu})^{1/n} = A(h\boldsymbol{\nu}-E_g) \quad (4)$$

Where α is the absorption coefficient, h is Planck's constant, $\boldsymbol{\nu}$ is frequency in Hertz, A is a proportionality constant, n is the Tauc exponent, and E_g is the band gap energy in electron volts[24]. By taking UV-Vis spectra and observing the change in the material's ability to absorb light (for example, absorbance and band edge change), it is possible to reveal the crystallinity and morphology change during semiconductor degradation.

In this project, steady-state photoluminescence (PL) spectroscopy has also been used to further study the degradation mechanism of the perovskites. In PL spectroscopy, electrons are excited with a light source, and photoluminescence is emitted when excited electrons emit a photon as they relax to lower energy states. Photons emitted at different wavelengths may indicate a change in bandgap. A larger band gap relaxation will emit a higher energy (short wavelength) photon. The emitted electron's light intensity and wavelength are measured by the

instrument and plotted on a spectrum. The PL intensity is significantly affected by the so called "nonradiative recombination", where a photoexcited electron recombines with a hole in the ground state without releasing a photon. Nonradiative recombination is generally facilitated by trap states (formed by the defects) in the perovskites[25]. In perovskite solar cells, however, the majority of the excited charge carriers (electrons and holes) will be transferred to the ETL and HTL, bypassing the radiative and nonradiative recombination. Therefore, by recording the PL spectra of the perovskite and perovskite/E(H)TL thin films, and monitoring their PL intensity and PL peak position change, it is possible to reveal the change of the defect density in the perovskite thin films and the charge transfer efficiency at the perovskite/ETL and perovskite/HTL interfaces during perovskite degradation.

Chapter 2: Materials and Methods

2. 1 Glass substrate preparation

Glass substrate from Thermo Scientific was prepared by cleaning with a 75% ethanol solution, and then was placed in a UV-Ozone cleaner (BioForce Nanosciences Procleaner) for 15 minutes to remove a maximum amount of surface contamination and increase thin film adhesion to the surface of the substrate.

2.2 TiO_2 Film Preparation

0.0048 g of titanium dioxide paste (DSL 18NR-AO, Sun Coast) was dissolved in 5.00ml terpineol and 5.00ml ethanol by manual agitation to form a 0.5M solution. Plates were annealed

at 500^0C for 15 minutes, and appeared clear and colorless to the eye. TiO_2 films were spin-coated at 4000rpm for 60 seconds, and annealed at 500^oC for 15 minutes.

2.3 Spiro-OMeTAD Film Preparation

0.3165g of Spiro-OMeTAD powder (Sigma Aldrich) was dissolved in 5.00ml of chlorobenzene and left to dissolve for 30 minutes to prepare a spiro-OMeTAD solution. Spiro-OMeTAD films were spin-coated at 4000 revolutions per minute (rpm) for 60 seconds, and annealed at 80^oC for 10 minutes. The recipe of the Spiro-OMeTAD solution was adapted from Mattiello[29].

2.4 $MAPbI_3$ Film Preparation

A recipe for $MAPbI_3$ solution was adapted from[30] and prepared as follows: 0.1569g MAI, 0.4599g PbI2, 0.318g DMF, 0.318g DMSO. Once the solution was prepared, it could be spin-coated. Both perovskite films were prepared using the same spin coating method in four steps. First, the plate is spun at 1000 rpm for 30 seconds. Second, it is spun at 6000 rpm for 40 seconds with 40 microliters of antisolvent dripped during the last 5 seconds. Third, a 10 second rest step. Fourth, the plate is spun at 6000 rpm for 10 seconds, with 40 microliters of antisolvent dripped during the last 5 seconds. Plates were annealed for 2 minutes at 80^oC.

In the spin-coating process, ethanol is used as an anti-solvent. An anti-solvent is a solvent, typically used during spin-coating, that increases crystal size and decreases point defects, to benefit the electronic properties of the perovskite[31].

2.5 $MAPbBr_3$ Film Preparation

0.0784g MABr was combined with 0.2305 $PbBr_2$ and 1:1 DMF:DMSO to prepare the solution. The solution went on as a clear liquid, and annealed to an orange solid after spin-coating.

2.6 Characterization

All the thin film samples were annealed on a Corning hot plate before placed under an Oriel LCS-100 Small Area Solar Simulator for aging under a standard 1 sun solar radiation. UV vis and PL spectra were taken for the samples at different aging times. UV-Visible spectroscopy was conducted on a VWR UV-1600PC, UV/Visible Spectrophotometer and associated software. UV-Vis spectra were measured over a wavelength range of 350-900 nanometers. This range was selected based on the range of the spectrophotometer, and the expected range of absorption from samples. PL spectroscopy was conducted on a Horiba Scientific FluoroMax-4 Spectrofluorometer and FluorEssence software. PL of the perovskite films were collected from 450-800 nanometers with an excitation wavelength of 400 nanometers.

2.7 Optimization of concentration and spinning method

One major obstacle to this project was combatting film roughness after spin-coating.

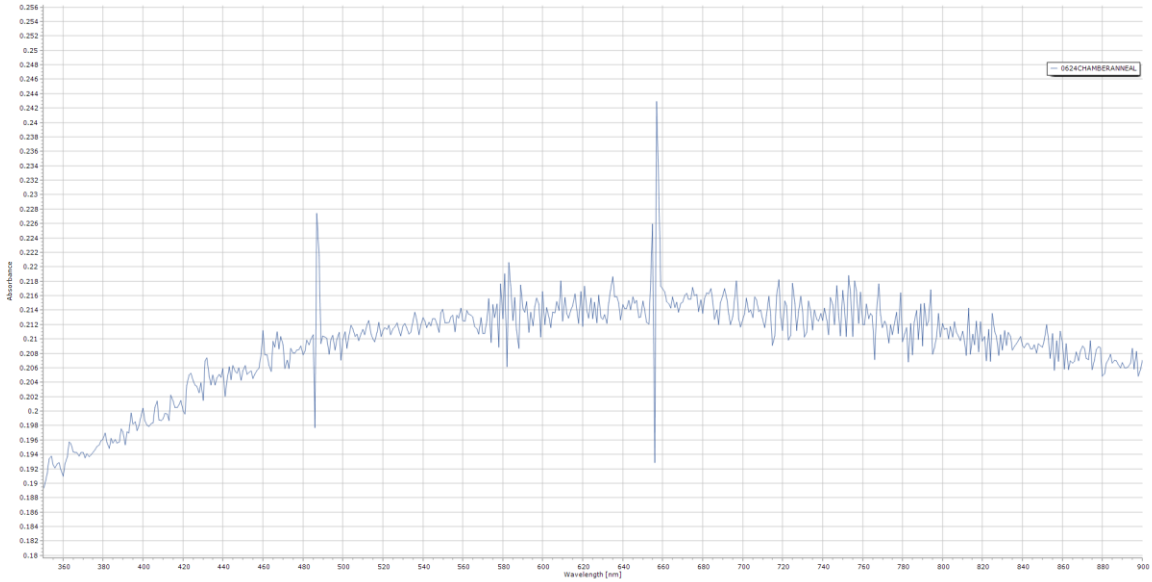

Figure 5: A single layer $MAPbI_3$ film with a high degree of surface roughness.

For a uniform perovskite thin film with good crystallinity, its absorption spectrum typically includes a broad peak in the shorter wavelength part of the spectrum, and for specifically $MAPbI_3$, a characteristic absorption peak near 500 nm[32]. There is also typically low

absorption at wavelengths higher than the band edge, or above 780 nm. However, as shown In figure 5 for the absorption spectrum of $MAPbI_3$ thin film fabricated by a one-step spin coating of precursor solution, there are low absorbances where a peak for the perovskite ought to be, around 500 nm, and stronger absorbances above 800 nm, where little to no absorbance is expected. This is a strong indication that the perovskite thin film formed by the conventional one-step spin coating procedure is highly inhomogeneous.

On the rough surface of a perovskite thin film, the film covers imperfectly, leaving some areas thin or uncovered, and others much thicker. In the thin regions, light will pass through with some loss of energy. In the thick regions, the density is high enough to absorb almost all the light. The spectra of thin films with a high degree of roughness do not necessarily correlate to the material's absorptivity, instead showing "constant optical density" across the range of spectroscopic wavelengths[33]. Furthermore, a rough thin film surface will cause strong wavelength-independent light scattering during the absorption measurement, and this effect also contributes to the formation of a "featureless" spectrum as shown in Figure 5.

This project adopts a shorthand for estimating the roughness based on a film's UV-Vis spectrum: the absorbance of the film at 900 nm, divided by the absorbance of the film at 350 nm. The smaller that ratio, the smoother the film is estimated to be.

To combat surface roughness, four spin-coating methods were adapted from the literature and tested in the lab, to see if any of the methods could produce the quality of results desired.

Table 1: Comparison of spin-coating methods.

Spin Coating and Anti-Solvent	Nishimura-Behera[35] Method	CASM[36]	Prenucleation Method[37]

Procedure (SCASP)[34]			
1. 1000 rpm, 10s, 1000 rpm/s 2. 4000 rpm, 30s, 1200 rpm/s. Last 10s, 100µl of antisolvent	1. 6000 rpm, 50s, 2000 rpm/s. After 10s elapsed, 1ml antisolvent.	1. 1000 rpm for 10s, 1000 rpm/s 2. 4000 rpm for 45s. Drip 80µl last 20s.	1. 1000 rpm, 30s, 1000 rpm/s. 2. 6000 rpm, 2000 rpm/s, 40s, drip 40 µl antisolvent last 5s 3. 0 rpm, 10s 4. 6000 rpm, 2000 rpm/s, 10s. Drip 40 µl antisolvent last 5s.

UV-Vis spectra of each sample were compared.

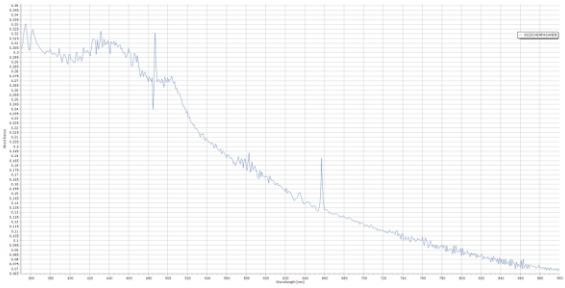

Figure 6: UV-Vis spectrum of a sample made with the SCASP procedure.

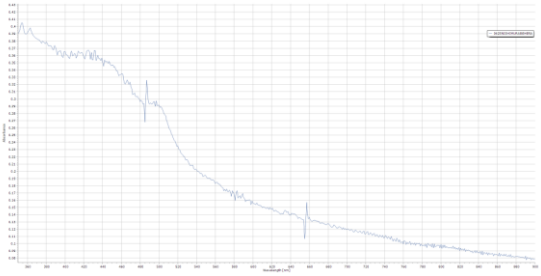

Figure 7: UV-Vis spectrum of a sample made with the Nishimura-Behera method.

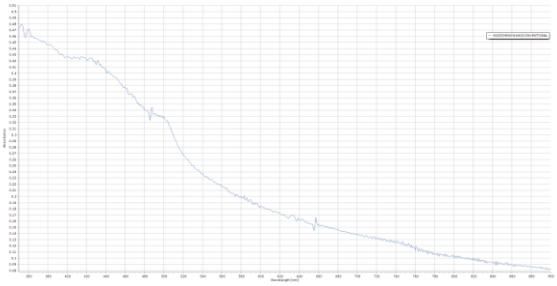

Figure 8: UV-Vis spectrum of a sample made with the conventional method.

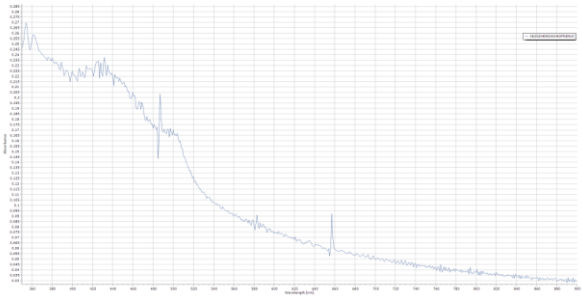

Figure 9: UV-Vis spectrum of a sample made with the prenucleation method.

The primary differences between the four methods are the antisolvent amount and timing. The role of an anti-solvent in a procedure like spin-coating is to remove the original solvent to improve nucleation of a perovskite thin film. The amount of time the perovskite film is in contact with the anti-solvent matters. The antisolvent amount also matters. Too long a contact time, and defects will form in the crystal, and too much anti-solvent can alter the crystal morphology[38]. The SCASP procedure has 10s of contact time and 100µl of antisolvent. The Nishimura-Behera method has 10s of contact time and 1ml of anti-solvent. The conventional method has 20s of contact time and 80µl of antisolvent. The prenucleation method has two 40µl and 5s aliquots spaced out throughout its procedure. The smaller amounts of anti-solvent and contact time were likely why the prenucleation method gave the smoothest samples. We can also compare the absorbances at 900 and 350 nanometers as an approximation of surface roughness. The SCASP method, shown in figure 6, has a roughness of ⅓. The Nishimura-Behera method, shown in figure 7, yields a roughness of ¼. The conventional method from Zhang et al. in figure 8 has a roughness of 1/9. The prenucleation method, shown in figure 9 has a roughness of 1/10, proving to be the method best suited for reducing surface roughness.

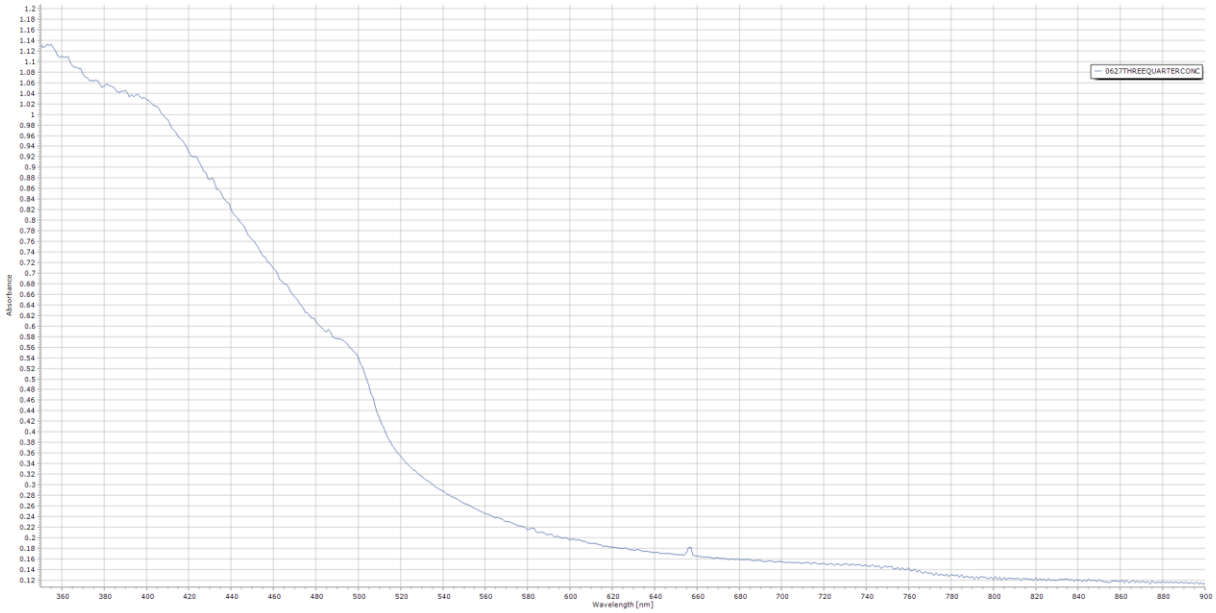

Figure 10: Example of a UV-Vis spectrum of a good quality perovskite sample.

In figure 10, the absorption spectrum of a single layer perovskite film produced by the prenucleation method with optimized solution concentration and film thickness, a gentle peak for the perovskite at 500 nm is visible, and there are low absorbances above 800 nm, both desirable qualities in UV-Vis spectra for this project.

Chapter 3: Investigating the degradation processes of $MAPbI_3$ perovskite with UV-Vis spectroscopy

Methylammonium lead iodide was one of two perovskites selected for examination in this project, due to it being highly common in lead halide perovskite solar cells, and for its relatively high level of chemical stability under ambient conditions[12].

To examine interfacial effects on methylammonium lead iodide, four different types of samples were made. First, a sample of only the perovskite ($MAPbI_3$) on the glass substrate to understand what its behavior was in the conditions of the lab without any interfaces. Second, a layer of TiO_2 underneath a layer of the perovskite, namely $MAPbI_3/TiO_2$. Third, a layer of the perovskite underneath a layer of the spiro-OMeTAD (spiro-OMeTAD/$MAPbI_3$). For this sample, the order of the layer was changed because if the spiro-OMeTAD were underneath the perovskite, it would dissolve in the solvents used in the perovskite solution, destroying the sample before it could be measured. The fourth sample consisted of, in ascending order: the glass substrate, a layer of TiO_2, a layer of perovskite, and a layer of spiro-OMeTAD (spiro-OMeTAD/ $MAPbI_3/TiO_2$).

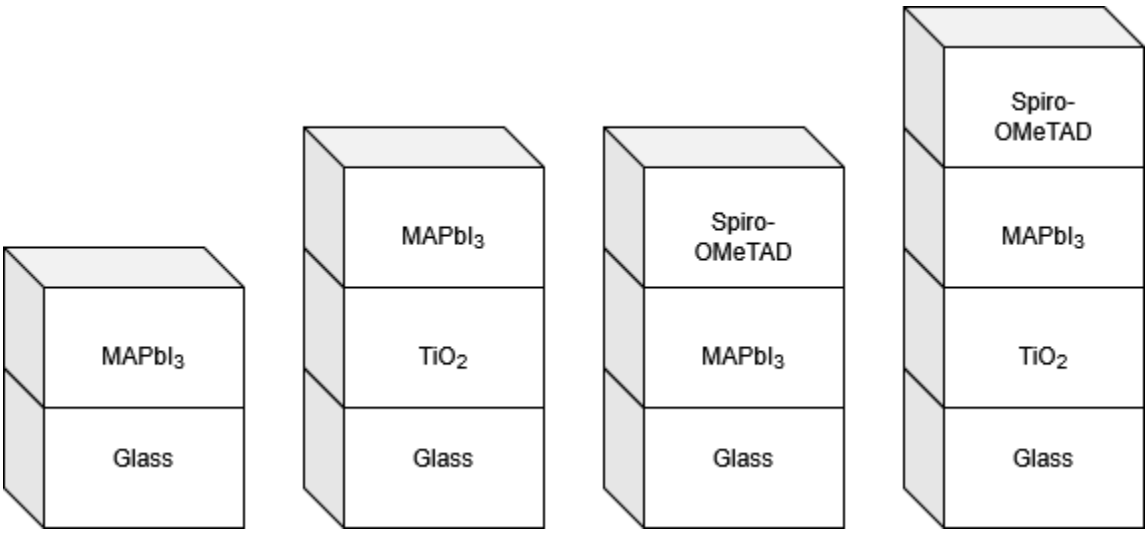

Figure 11: Layering order of experimental samples.

The process of making the films starts with cleaning the glass substrate in 75% ethanol solution, and cleaning it with the UV ozone cleaner for 15 minutes. Once the substrate was ready, it was placed into the spin-coater, the solution added, and the spin sequence engaged. Anti-solvent treatments took place during the spin-coating step. After spin coating, samples were annealed for the prescribed time and temperature. If the sample required additional layers, it would return to the spin coating step. If not, it would go into the spectrophotometer for measurement. Once measurements were complete, the sample would be aged under 1 sun illumination. The measurement and aging steps repeated up to 36 hours.

PL spectra of the $MaPbI_3$ samples were not obtained due to its emission peak (around 780nm) being outside our spectrometer's measurement range. The UV-Vis spectra of the $MAPbI_3$ samples are shown in Figure 12-15.

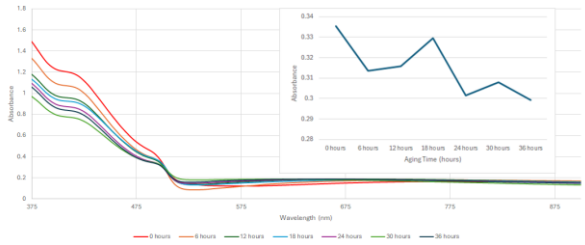

Figure 12: UV-Vis absorption spectra of the $MAPbI_3$ single layer sample with different aging times. The inset shows the change of absorbance values at wavelength of 500nm for the $MAPbI_3$ single layer sample with different aging times.

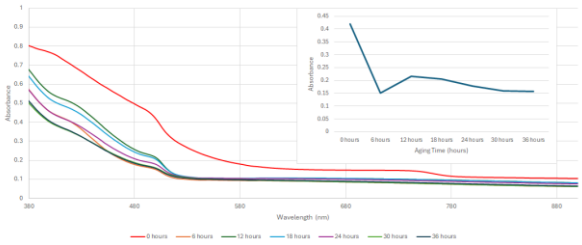

Figure 13: UV-Vis absorption spectra of the $TiO_2/MAPbI_3$ double layer sample with different aging times. The inset shows the change of absorbance values at wavelength of 500nm for the $TiO_2/MAPbI_3$ double layer sample with different aging times.

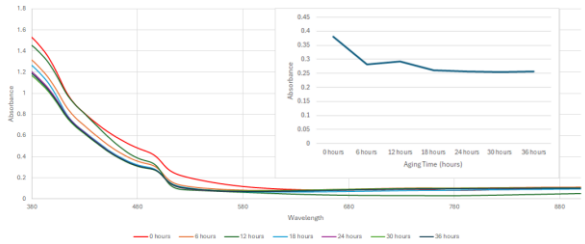

Figure 14: UV-Vis absorption spectra of the $MAPbI_3$/spiro-OMeTAD double layer sample with different aging times. The inset shows the change of absorbance values at wavelength of 500nm for the $MAPbI_3$/spiro-OMeTAD double layer sample with different aging times.

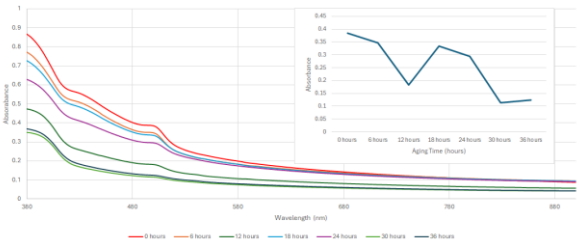

Figure 15: UV-Vis absorption spectra of the TiO_2/$MAPbI_3$/spiro-OMeTAD triple layer sample with different aging times. The inset shows the change of absorbance values at wavelength of 500nm for the TiO_2/$MAPbI_3$/spiro-OMeTAD triple layer sample with different aging times.

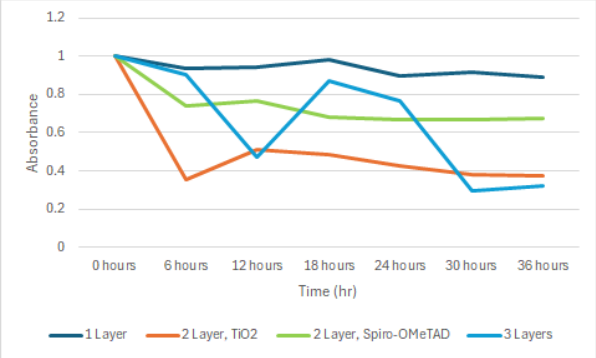

Figure 16: Normalized absorbance (at wavelength of 500nm) vs aging times for $MAPbI_3$, $MAPbI_3$/TiO_2, spiro-OMeTAD/$MAPbI_3$, and spiro-OMeTAD/$MAPbI_3$/TiO_2, respectively. To facilitate easy comparison, the absorbances at 0 hours are normalized to 1 for all four samples.

Figure 12 demonstrates the typical absorption spectra of $MAPbI_3$ which include an absorption edge at around 780nm and a very broad absorption band at UV-visible range. It is also

shown that the overall absorption intensity of the broad band in the UV-vis range decreases with increasing aging time, suggesting degradation of the perovskite film. However, we don't observe significant change of absorption peak and absorption edge positions. Therefore, the typical degradation products like hydroiodic acid (HI) and lead II iodide (PbI_2) are not clearly identified. This could be explained by the fact that the initial absorption band of the unaged perovskite sample is quite broad and the peaks associated with the degradation products are within the broad peak. Furthermore, as a direct band semiconductor, $MAPbI_3$ has high absorption coefficient, which could easily overpower the absorption of the decay products. As shown in Figure 12, there is a slight increase of absorption in the range of 550-650nm which might be related to the degradation products.

It is also shown in Figure 12 that the absorption of the perovskite does not solely decrease with aging time. The absorption spectrum goes "up" and "down" with increase of aging time. The inset in Figure 12 clearly shows an unsteady decay of the absorbance of $MAPbI_3$ perovskite film at the wavelength of 500nm. This cannot be simply attributed to experimental errors since the effect is consistently observed for all samples. Instead, this observation could be attributed to a "light annealing" effect on the perovskite thin films[39]. It is well known that a spin-coated perovskite thin film is amorphous and thermal annealing can significantly increase the crystallinity of the film. Perovskite thin films with better crystallinity show stronger light absorption. It has been reported that exposing the perovskite to light might have a similar effect as thermal annealing. The unsteady decay of the absorbance of the $MAPbI_3$ perovskite film during aging can be explained by the two distinct effects from light exposure. First, light induced degradation deteriorates the perovskite structure and reduces light absorption; Second, the light annealing effect increases the

crystallinity of perovskite thin film and enhances light absorption. And the different dynamics of the two opposite effects could lead to unsteady degradation of perovskite under light illumination.

Figure 13 shows absorption spectra of the $MAPbI_3/TiO_2$ double layer thin film taken at different aging times. The absorption spectra of $MAPbI_3/TiO_2$ double layer thin film is similar to that of the $MAPbI_3$ single layer sample, because the absorption of TiO_2 thin film is mainly in the UV range (wavelengths shorter than 400 nm). Similar to the $MAPbI_3$ single layer sample, there is significant absorbance decrease during aging for the $MAPbI_3/TiO_2$ double layer thin film. It is also shown in figure 13 (and inset) that the decay of absorbance is unsteady. It suggests the interplay of the two light-induced effects also affects the degradation of the $MAPbI_3/TiO_2$ double layer thin film. However, we observe significantly greater reduction of absorption in $MAPbI_3/TiO_2$ compared with the $MAPbI_3$ single layer sample. For example, the absorbance at 500 nm for $MAPbI_3/TiO_2$ double layer (as shown in Figure 16) after 36 hours aging is around 40% of its initial value, compared to around 90% for the $MAPbI_3$ single layer. The greater reduction in absorbance of $MAPbI_3/TiO_2$ double layer thin film suggests that the TiO_2 layer can actually accelerate the degradation processes of $MAPbI_3$ perovskite top layer under light illumination.

The effect of the TiO_2 ETL layer on the degradation of $MAPbI_3$ perovskite can be explained by the ion migration mechanisms in perovskite thin films[40]. It is well known that $MAPbI_3$ perovskite has a mixed electronic/ionic conducting nature due to low activation energies for ion formation and migration, especially for I^-. It has also been reported that ion migration in thin films can be facilitated by photon energy[41]. In a $MAPbI_3$ single layer film the ions migration or diffusion is directionless. However, in a $MAPbI_3/TiO_2$ sample ions can selectively migrate

towards the TiO_2 layer because the ions, mainly I^-, can form a strong bonding with the uncoordinated Ti^+ ions on the mesoporous TiO_2 surface[42]. We hypothesize that continuous diffusion of I^- towards TiO_2 driven by photon energy and accumulation of them at the TiO_2 interface through bond formation with Ti^+ accelerates the degradation process of $MAPbI_3$ perovskite under light illumination.

Figure 14 shows the absorption spectra of the spiro-OMeTAD/$MAPbI_3$ double layer thin film at different aging times. The absorption of spiro-OMeTAD is in the UV range, between 305 and 385 nm depending on the solvent[43]. Therefore, the absorption spectra of spiro-OMeTAD/$MAPbI_3$ is fairly similar to the spectra of $MAPbI_3$ single layer sample in our recorded wavelength range. Like the $MAPbI_3$ spectrum, there is absorbance decrease during the aging of samples, though less pronounced than that of the TiO_2/$MAPbI_3$. As in the samples discussed previously, the decay of the two layer $MAPbI_3$/spiro-OMeTAD thin film is unstable. The opposing light effects discussed earlier in this chapter also affect the degradation of the $MAPbI_3$/spiro-OMeTAD thin film. The $MAPbI_3$/spiro-OMeTAD thin film experiences greater reduction in absorbance than the single layer $MAPbI_3$ film, about 60% at 36 hours aging compared to around 90% for the single layer $MAPbI_3$ film, indicating that the presence of spiro-OMeTAD may accelerate the degradation of $MAPbI_3$ under illumination.

The effect of the spiro-OMeTAD HTL on $MAPbI_3$ degradation can also be explained by ion migration in perovskite thin films[44]. $MAPbI_3$ is a mixed ionic and electronic conductor because the material has lower energy thresholds for ion migration than other OMH perovskites. In a two layer sample like $MAPbI_3$/spiro-OMeTAD, the I^- and MA^+ ions will form MAI[46] and seek to diffuse into spiro-OMeTAD. The accumulation of I^- at the interface, and I^- diffusion into

spiro-OMeTAD accelerates the degradation of $MAPbI_3$[45]. Unlike TiO_2 ETL, which has a mesoporous structure and therefore provides a large interfacial area, spiro-OMeTAD HTL has a planar surface which provides less surface area for ion accumulation. It is also possible that the association rate between I^- and $OMeTAD^+$ is lower than that between I^- and Ti^+. As a result, spiro-OMeTAD HTL has lesser effect on $MAPbI_3$ degradation compared to TiO_2.

Figure 15 shows the absorption spectra of the TiO_2/$MAPbI_3$/spiro-OMeTAD three layer thin film at different aging times. The spectrum of the three-layer thin film has elements of both the TiO_2 interface sample, and spiro-OMeTAD interface sample. Similar to the other samples, figure 15 demonstrates overall loss of absorbance with intermittent gains in absorbance. Light annealing and light degradation affect the three-layer sample in similar ways to the individual interface samples. The three-layer thin film shows absorbance losses down to approximately 35% of its original value at 36 hours aging. These losses are most similar to the $MAPbI_3$/TiO_2 double layer thin film, which decayed to approximately 40% of its original absorbance after 36 hours aging.

The TiO_2/$MAPbI_3$/spiro-OMeTAD three-layer thin film does not experience any new ion migratory effects. Because it experiences degradation effects at two interfaces, there is a greater degree of degradation over the same aging time as the other samples. However, as we discussed earlier, the overall degradation rate (at 36 hours) of the three-layer sample is similar to the TiO_2 two-layer sample. This can be explained by a stronger light annealing effect on the three layer thin film as demonstrated by strong absorbance recovery at 18 hours of aging time as shown in figure 16. This may be attributed to the fact that the crystals are confined to a small space due to having two material interfaces on either side of the perovskite layer. The physical confinement of

the crystals may produce a stronger annealing effect, and decelerate the degradation processes of the perovskite under light illumination.

In summary, light induced degradation of $MAPbI_3$ is evident based on the UV vis absorption spectra taken at different aging times. The presence of TiO_2 and spiro-OMeTAD contribute to that degradation, TiO_2 more than spiro-OMeTAD. Iodine ions may diffuse into TiO_2 more quickly because it has a mesoporous structure, providing more Ti^+ and surface area at which to interact. The degradation of $MAPbI_3$ is related to iodine (and possibly lead) ions accumulation at the material interfaces.The triple-layer sample, which possesses two interfacial layers and both contribute the degradation of $MAPbI_3$, shows similar overall degradation rate as TiO_2 double layer sample. This is possibly due to stronger light annealing effect on the confined perovskite crystals in the three-layered sample, which partially counters the light degradation effect.

Chapter 4: Investigating the degradation processes of $MAPbBr_3$ perovskite with UV-vis and PL Spectroscopy

$MAPbBr_3$ is the second perovskite selected for this project. The primary difference between $MAPbBr_3$ and $MAPbI_3$ is that the bromide perovskite has a cubic crystal structure at room temperature[5]. $MAPbBr_3$ has a slightly wider band gap than that of $MAPbI_3$, 2.3 eV as compared to 1.6 eV. The band gap is wider in the bromide OHMP because the greater bond energy in the Pb-Br bond[20] creates greater separation between the electrons bound in the structure, and electrons free to move in the structure[46, 47]. MAPbBr3 is more resistant to degradation factors like illumination, water, and oxygen. The UV-Vis peak of $MAPbBr_3$ is located at approximately 520 nm, and the PL peak is located at approximately 540 nm[48].

The $MAPbBr_3$ for this experiment was synthesized from MABr and $PbBr_2$. Following similar procedures as $MAPbI_3$, four samples including $MAPbBr_3$ single layer, $MAPbBr_3/TiO_2$ double layer, spiro-OMeTAD/$MAPbBr_3$ double layer, spiro-OMeTAD/$MAPbBr_3/TiO_2$ triple layer were fabricated and measured with both ultraviolet-visible absorption spectroscopy and steady-state photoluminescence (PL) spectroscopy.

4.1 UV-Vis absorption spectroscopy

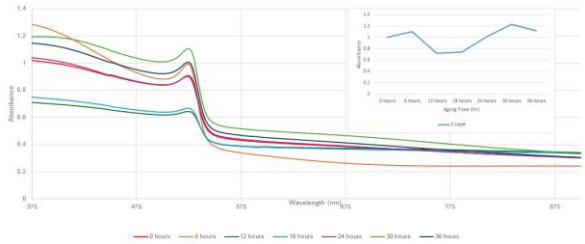

Figure 17: UV-Vis absorption spectra of the $MAPbBr_3$ single layer sample with different aging times. The inset shows the change of absorbance values at 500 nm wavelength for the $MAPbBr_3$ single layer sample with different aging times.

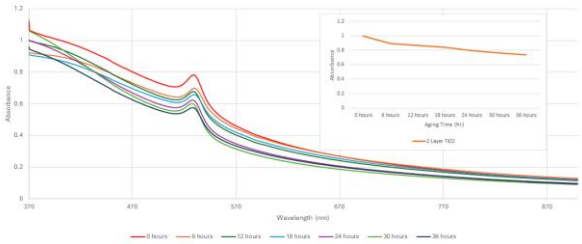

Figure 18: UV-Vis absorption spectra of the $TiO_2/MAPbBr_3$ double layer sample with different aging times. The inset shows the change of absorbance values at wavelength of 500nm for the $TiO_2/MAPbBr_3$ double layer sample with different aging times.

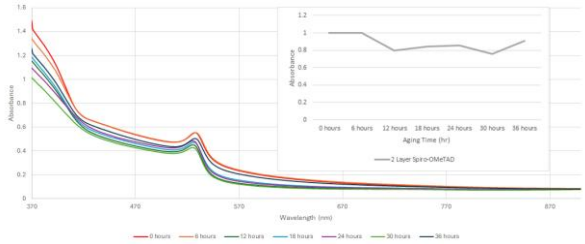

Figure 19: UV-Vis absorption spectra of the $MAPbBr_3$/spiro-OMeTAD double layer sample with different aging times. The inset shows the change of absorbance values at wavelength of 500nm for the $MAPbBr_3$/spiro-OMeTAD double layer sample with different aging times.

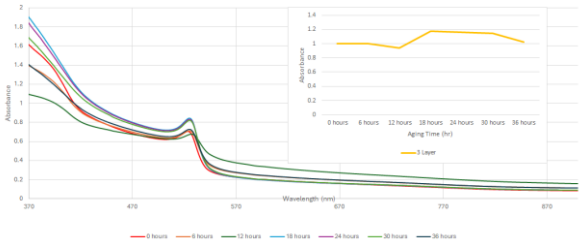

Figure 20: UV-Vis absorption spectra of the $TiO_2/MAPbBr_3$/spiro-OMeTAD triple layer sample with different aging times. The inset shows the change of absorbance values at wavelength of 500nm for the $TiO_2/MAPbBr_3$/spiro-OMeTAD triple layer sample with different aging times.

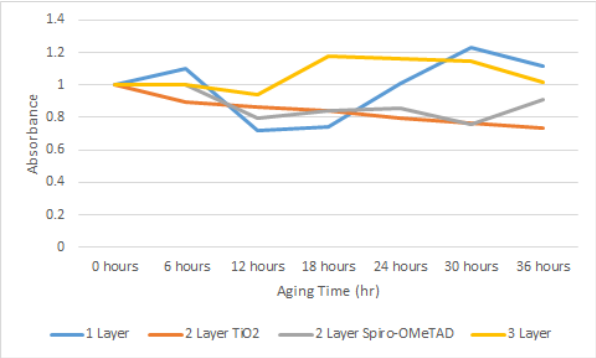

Figure 21: The change of absorbance values at wavelength of 500nm for figures 17-20. To facilitate easy comparison, the absorbances at 0 hours are normalized to 1 for all four samples.

Figure 17 demonstrates the typical absorption spectra of $MAPbBr_3$ which includes an absorption edge near 520 nm, a peak around 530 nm, and low absorbances beyond 600 nm[49]. Figure 17 also demonstrates an absorbance increase with increasing aging time, which suggests that the $MAPbBr_3$ film quality is improving. This could be explained by the light annealing effect discussed in chapter 3, and (recall back to chapter 1 of this thesis) the overall greater environmental stability of $MAPbBr_3$, which stands in contrast to the degradation of $MAPbI_3$ over 36 hours of aging. The peak position of the $MAPbBr_3$ thin film does not change over the aging time of the sample. The absence of a shift in the absorbance peak position does not conclusively confirm the formation of expected degradation products, such as $PbBr_2$.

However, the transition from hours 6 to 12 of aging in the $MAPbBr_3$ thin film clearly shows an absorbance decrease. It is proposed that once the $MAPbBr_3$ decays initially, after light exposure the remaining mass reorganizes, increasing its crystallinity and absorbance. The

unsteadiness in how the $MAPbBr_3$ film absorbance behaves is accounted for by the interplay between light driven degradation and light driven annealing.

Figure 18 shows absorption spectra of the $MAPbBr_3/TiO_2$ double layer thin film taken at different aging times. The spectrum in figure 18 is similar to that of the single layer $MAPbBr_3$ sample, except for stronger absorption in the ultraviolet part of the spectrum (wavelengths fewer than 400 nanometers) where TiO_2 absorbs. Unlike the $MAPbBr_3$ single layer spectrum, the $MAPbBr_3/TiO_2$ double layer thin film displays steady absorbance decrease, indicating a relatively steady degradation rate across the sample aging time. The two layer sample degrades to approximately 75% of its original value at 36 hours aging time, whereas the single layer sample gains to 110% of its original value over the same aging time. So apparently the TiO_2 layer accelerates the degradation of $MAPbBr_3$ when illuminated, which is similar to the behavior in the $MAPbI_3/TiO_2$ double layer thin film.

Like in $MAPbI_3/TiO_2$, the behavior of the TiO_2 layer within the $MAPbBr_3/TiO_2$ double layer thin film can be explained by ion migration toward the TiO_2 layer, and side reactions at the interface. Br^- ions will migrate toward the interface with TiO_2. Under illumination, the TiO_2 surface can also catalyze the formation of degradation products[50]. As a result, the light driven diffusion of bromide ions to the TiO_2 and accumulation at the interface accelerates the degradation of $MAPbBr_3$.

Figure 19 shows absorption spectra of the spiro-OMeTAD/$MAPbBr_3$ double layer thin film. They are similar to the $MAPbBr_3$ single layer spectra except for stronger absorption in UV due to additional absorption of spiro-OMeTAD in that part of the spectrum. The decay in absorbance is unsteady in figure 19 and its inset. The sample demonstrates overall decay to

around 90% of its original value, whereas the $MAPbBr_3$ single layer thin film increased absorbance up to 110% of its original. Similar to the samples discussed in chapter 3, the relationship between light annealing and light degradation explains the erratic increase and decrease behavior of the sample. The loss of absorbance in the presence of spiro-OMeTAD indicates that spiro-OMeTAD will contribute to the decay of a $MAPbBr_3$ perovskite layer in the presence of illumination.

The effect of the spiro-OMeTAD layer on the degradation of the $MAPbBr_3$ perovskite is governed by the same mechanism as the interaction between spiro-OMeTAD and $MAPbI_3$. Of note in the interaction between spiro-OMeTAD and $MAPbBr_3$ are much slower reaction kinetics[44].

Figure 20 is the absorption spectra of the TiO_2/$MAPbBr_3$/spiro-OMeTAD triple layer thin film. Unlike the $MAPbI_3$ triple layer thin film, the MAPbBr3 triple layer thin film shows absorbance recovery past its baseline measurement at 0 hours of aging. The light annealing effect is more pronounced on the more stable $MAPbBr_3$ structure; the TiO_2/$MAPbBr_3$/spiro-OMeTAD triple layer thin film keeps approximately 100% of its initial measurement after 36 hours of aging. However, at 36 hours of aging, the sample has lost around 20% absorbance from its maximum absorbance recorded at 18 hours. This absorbance loss demonstrates that the TiO_2/$MAPbBr_3$/spiro-OMeTAD triple layer thin film is still subject to the same degradation mechanisms discussed earlier in this chapter, but more resistant to them over a longer timeframe. The presence of TiO_2 and spiro-OMeTAD accelerate the observed degradation, TiO_2 more than spiro-OMeTAD, as they provide similar results across both perovskites. And similar to the TiO_2/$MAPbI_3$/spiro-OMeTAD, the interfacial behaviors of the TiO_2/$MAPbBr_3$/spiro-OMeTAD

triple layer thin film can also be attributed to light-driven ion migration toward material interfaces and potential side reactions at those interfaces that occur more slowly than the degradation of $MAPbI_3$. The interfacial interaction between TiO_2 and the bromide OHMP displays the most pronounced degradation, followed by the lesser, although contributing, influence of the spiro-OMeTAD interface. However, the interfaces establish a structural framework that facilitates increased crystallinity as a result of the light annealing effect; not all interfacial effects yield negative outcomes for the crystal.

In summary, based on the UV-Vis absorption spectra we observe $MAPbBr_3$ degrades at a relatively slower rate than $MAPbI_3$. The presence of TiO_2 ETL and spiro-OMeTAD HTL accelerate the degradation. The triple-layer sample, which possesses two interfacial layers and both contribute to the degradation of $MAPbBr_3$, shows very limited overall degradation due to stronger light annealing effect. The observation on $MAPbBr_3$ degradation under light illumination further supports our hypothesis that ion migration and accumulation at the ETL/HTL contributes to the degradation of perovskite solar cells.

4.2 Photoluminescence

A photoluminescence spectrum shows the radiative decay of electrons excited by photons. As shown in figure 22, photoexcited electrons decay either radiatively or non-radiatively. Radiative decay emits a photon with specific energy that displays on the recorded spectrum with a specific wavelength and intensity. The more photons that participate in radiative decay, the greater the PL intensity on the spectrum will be. As a result, high absorbance of

perovskites often leads to high PL intensity because more electrons are excited. The opposite is also true: the more photons participate in non-radiative decay, the lower PL intensity on the spectrum will be. The nonradiative decay is often facilitated by the deep trap states located in the band gap (as shown in figure 22). There are different types of defects in OMH perovskites, including vacancies (a space where there should be an atom in the lattice), impurities (an atom of the wrong species in the lattice), grain boundaries (misalignments between crystals), and surface defects, etc. These defects may create energy levels within the band gap of the host material. Shallow defects are located close to the conduction or valence bands within the band gap, where deep defects are located further away from the conduction and valence bands in the bandgap. Electrons trapped in shallow defects can escape those traps and recombine with the holes in the valence band and emit a photon (radiative decay). But the photons emitted by shallow traps generally have a slightly lower energy (longer wavelengths) than the photons emitted by electrons in the conduction band. Deep defects tend to create non-radiative decay, and can trap charge carriers, allowing the energy to dissipate as heat rather than light[51].

In perovskite solar cells, the OMH perovskite is sandwiched by ETL and HTL. Under light illumination, the photoexcited electrons in the perovskite may not recombine with the holes in the valence band. Instead, electrons could be transferred to ETL and holes transferred to HTL. Efficient charge transfer is a critical process to achieve high efficiency of light-to-electricity conversion in solar cells. Since charge transfer is a competing process for radiative recombination of photoexcited electrons, successful electron transfer to the ETL or hole transfer to the HTL will decrease the PL intensity of perovskite.

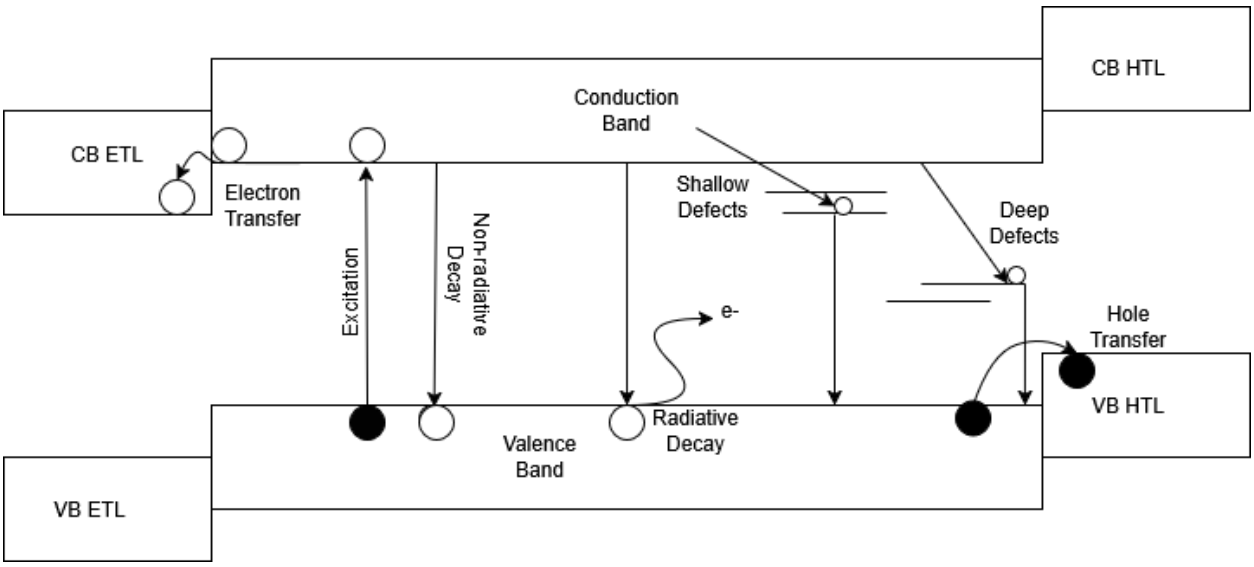

Figure 22: A diagram demonstrating different decay pathways for photoexcited electrons inside the OMH perovskites.

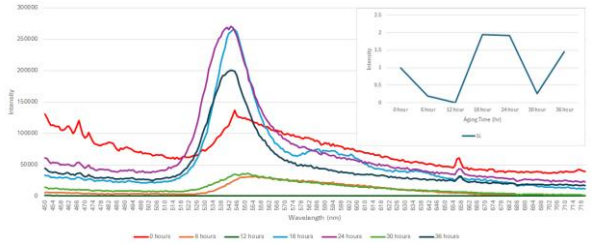

Figure 23: PL intensity spectra of the $MAPbBr_3$ single layer sample with different aging times. The inset shows the PL peak intensity change at the different aging times for $MAPbBr_3$. The PL peak intensity is normalized to 1 at 0 hours.

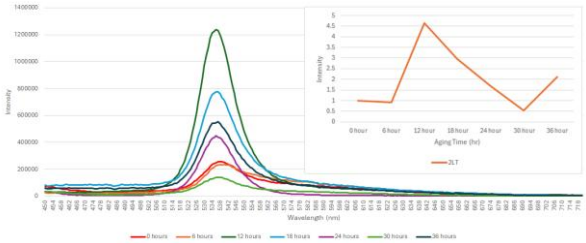

Figure 24: PL intensity spectra of the $TiO_2/MAPbBr_3$ double layer sample with different aging times. The inset shows the PL peak intensity change at the different aging times for the $TiO_2/MAPbBr_3$ double layer sample. The PL peak intensity is normalized to 1 at 0 hours.

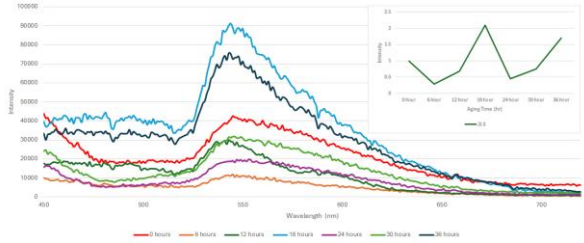

Figure 25: PL intensity spectra of the

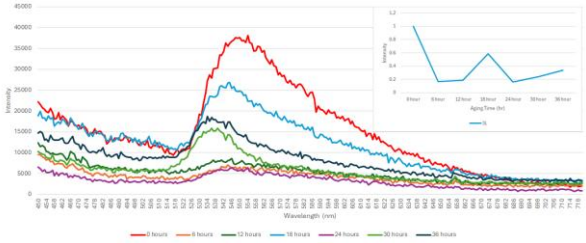

Figure 26: PL intensity spectra of the

$MAPbBr_3$/spiro-OMeTAD double layer sample with different aging times. The inset shows the PL peak intensity change at the different aging times for the $MAPbBr_3$/spiro-OMeTAD double layer sample with different aging times. The PL peak intensity is normalized to 1 at 0 hours.

TiO_2/$MAPbBr_3$/spiro-OMeTAD triple layer sample with different aging times. The inset shows the PL peak intensity change at the different aging times for TiO_2/$MAPbBr_3$/spiro-OMeTAD triple layer sample with different aging times. The PL peak intensity is normalized to 1 at 0 hours.

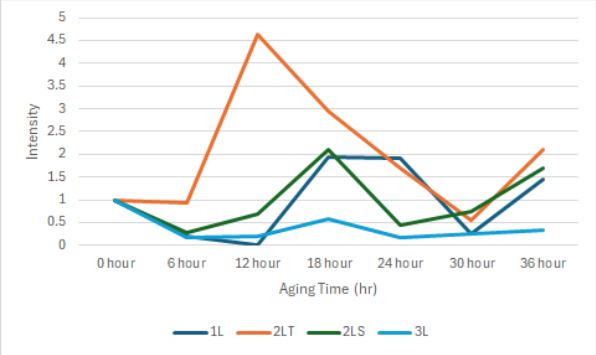

Figure 27: The change of intensity values at peak wavelength for figures 23-26. The PL peak intensity is normalized to 1 at 0 hours.

Figure 23 shows the PL spectra of $MAPbBr_3$ single layer thin film taken at different aging times. The spectra of $MAPbBr_3$ include a single emission band with peak wavelength at around 540 nm. The inset of figure 23 clearly shows the PL peak intensity of $MAPbBr_3$ fluctuates with increased aging time. As discussed earlier, the PL intensity is affected by light absorption and trap-assisted nonradiative recombination. By comparing the inset of figure 23 and the inset of figure 17, we find that PL intensity doesn't show much correlation with absorbance. For example, after the first 6 hours of aging, the absorbance increases slightly while the PL intensity decreases significantly. Therefore, the PL intensity seems to be dominated by the nonradiative decay, which is closely related to trap (defects) density. There are a variety of

defects in perovskite thin films including point defects (for example, I^-), grain boundary, and surface defects (for example, dangling bonds). Those defects form either shallow or deep traps for charge carriers (electrons and holes). A photoexcited electron trapped in shallow traps can still undergo radiative decay and emit a photon with energy slightly smaller than band gap. From the normalized the PL spectra shown in figure 27, we clearly observe that the emission band in the PL spectrum at 6 hours is broader and the peak position is slightly red shifted compared to the PL spectrum taken at 0 hour, which indicates more shallow traps are generated during the first 6 hours of aging. Although the exact nature of the shallow and deep traps in perovskites are not well understood, it's fair to assume the depth of trap states maintain a certain distribution in the band gap of perovskite. If there are more shallow traps in the perovskite after aging, there are likely more deep traps. This is consistent with the fact that the PL peak intensity decreases from 0 hour to 6 hours because the deep traps generated during aging facilitate nonradiative recombination and quench photoluminescence. This assumption is further confirmed by the PL data collected at other aging times. For example, at 18 hours, when the PL intensity increases (shown in the inset of figure 23), the PL emission band becomes narrower and slightly blue-shifted (shown in figure 27), suggesting lower trap density over that aging period.

In summary, PL of $MAPbBr_3$ is dominantly affected by the trap density in the thin film. As discussed earlier, light illumination will lead to two opposite effects on perovskite thin film. First the light induced degradation will generate more defects, and second, the light annealing effect will lead to better crystallinity and lower defect density. As a result, the defect density in the perovskite thin film could fluctuate during different aging times and leads to fluctuating photoluminescence intensity.

Figure 24 shows the PL spectra of $MAPbBr_3/TiO_2$ double layer thin film taken at different aging times, which have a similar emission band peaking at around 540 nm as the spectra of $MAPbBr_3$ single layer because the mesoporous TiO_2 is not emissive under excitation at 400 nm. The inset in figure 24 shows significant PL peak intensity fluctuation with increase of aging time, which is also similar to the $MAPbBr_3$ single layer thin film. As we discussed above, the PL intensity is dominated by the deep trap-assisted nonradiative recombination and the fluctuation of PL intensity for the $MAPbBr_3$ single layer thin film is attributed to the fluctuation of the trap density in the perovskite during different aging times. Here we also observe a similar effect of trap density on PL intensity. For example, the PL intensity increases more than 4 fold from 0 hours to 12 hours in figure 14. And during the same period of aging time the emission bandwidth at 12 hours shows significant reduction compared to that of the 0 hours spectrum, suggesting great reduction of trap density. However, the trap density doesn't seem to play a dominant role as it does for the $MAPbBr_3$ single layer. For instance, from 0 hours to 6 hours, we observe nearly no PL intensity change, but an obvious increase of bandwidth, which suggests an increase of trap density. Figure 18 shows that the absorbance $MAPbBr_3/TiO_2$ double layer thin film steadily decreases over aging, which indicates absorption change is also not a significant factor in determining the PL intensity. Here, we argue that charge transfer, another photophysical process which is in close relationship with photoluminescence (figure 22), plays a significant role in determining the PL intensity of $MAPbBr_3/TiO_2$. Unlike in $MAPbBr_3$ single layer thin film, there is a heterojunction interface formed between $MAPbBr_3$ and TiO_2 in the double layer sample, and under illumination an efficient electron transfer from $MAPbBr_3$ and TiO_2 is expected due to favorable energy band alignment. Since electron (charge) transfer is a competing

process for radiative recombination, a reduction of charge transfer efficiency will enhance PL intensity of the perovskite. As we have discussed earlier, the ions (like I^-) migrated to the TiO_2 interface will accumulate in the interfacial area by forming a strong bond with TiO_2 surface. The accumulated ion layer could form a potential barrier for an efficient electron transfer from perovskite to TiO_2, and hence increase the PL intensity of $MAPbBr_3/TiO_2$ double layer thin film.

To summarize, the PL spectra of the $MAPbBr_3/TiO_2$ double layer thin film is affected by both defect density and charge transfer. The relatively steady decrease of absorbance of the sample, as shown in figure 18 likely indicates that absorbance is not a determining factor for PL intensity. Fluctuations in the PL intensity throughout the aging time of the sample indicates fluctuating defect density and charge transfer efficiency over the same time period. The $MAPbBr_3/TiO_2$ double layer thin film shows immense increase in the PL intensity at certain aging times, suggesting ion accumulation at the TiO_2 interface can form a certain type of physical barrier reducing the electron transfer rate from $MAPbBr_3$ to TiO_2.

Figure 25 is the PL spectra of spiro-OMeTAD/$MAPbBr_3$ double layer thin film taken at different aging times, and no emission from spiro-OMeTAD is detected under excitation wavelength at 400 nm[51]. The inset in figure 25 shows a fluctuating PL intensity, in a pattern similar to the $MAPbBr_3$ single layer sample (figure 27). The maximum PL enhancement (around 100%) is not even close to what we observed for the $MAPbBr_3$ /TiO_2 (around 360%). And the normalized PL spectra shown in figure 29 shows change of bandwidth of emission band with aging time. All the observations suggest that trap (defect)-assisted nonradiative recombination plays a more dominant role than charge (hole) transfer in determining the PL intensity of spiro-OMeTAD/$MAPbBr_3$.

Under light illumination, efficient hole transfer is expected from $MAPbBr_3$ to spiro-OMeTAD due to a favorable energy band alignment as shown in Figure 22. Accumulation of ions at the HTL interface may also form an energy barrier for the hole transfer and consequently enhance PL intensity, just like the huge PL enhancement we observed for the $MAPbBr_3/TiO_2$. However, the PL enhancement is much smaller for the spiro-OMeTAD/$MAPbBr_3$ sample indicating that the ion accumulation effect isn't as pronounced in this sample as in the $MAPbBr_3/TiO_2$ sample. This is consistent with our conclusion based on the UV-Vis absorption spectroscopy results for the same double layer sample.

Figure 26 presents the PL spectra of spiro-OMeTAD/$MAPbBr_3/TiO_2$ triple layer thin film taken at different aging times. The inset in figure 26 shows mild fluctuating behavior of the PL peak intensity over the aging period. As shown in figure 27, this is the only sample which doesn't have any PL enhancement over the entire aging procedure. The normalized PL spectra shown in figure 31 clearly indicates gradual bandwidth narrowing and peak position blue-shifting over aging time, suggesting a strong light annealing effect which improves the perovskite crystallinity and reduces defects density. This is consistent with the enhanced absorption of the sample we observe in figure 20. However, the combination of an increased absorbance and a reduced defect density does not lead to any PL enhancement for the triple-layer sample. A reasonable explanation for this observation is that the improved crystallinity of the perovskite due to light annealing facilitates the charge transfer at both ETL and HTL interfaces, and even the ion accumulation at the interfaces seems not to slow down the transfers. As a result, the more efficient charge transfer prevents any PL intensity enhancement occurring during aging.

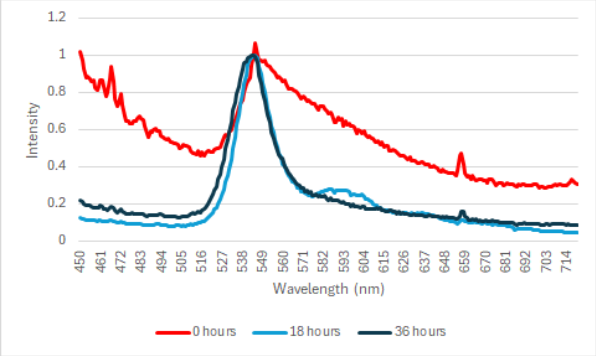

Figure 28: Normalized PL intensity spectra of the $MAPbBr_3$ single layer sample with different aging times.

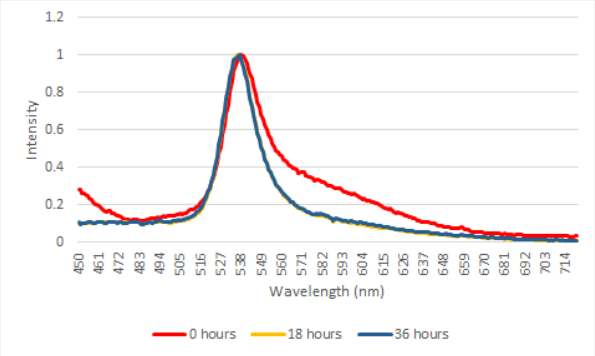

Figure 29: Normalized PL intensity spectra of the $TiO_2/MAPbBr_3$ double layer sample with different aging times.

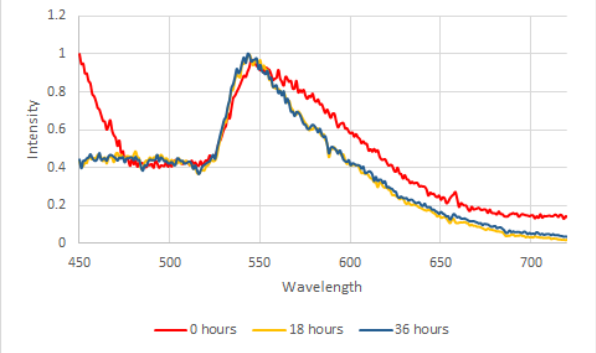

Figure 30: Normalized PL intensity spectra of the $MAPbBr_3$/spiro-OMeTAD double layer sample with different aging times.

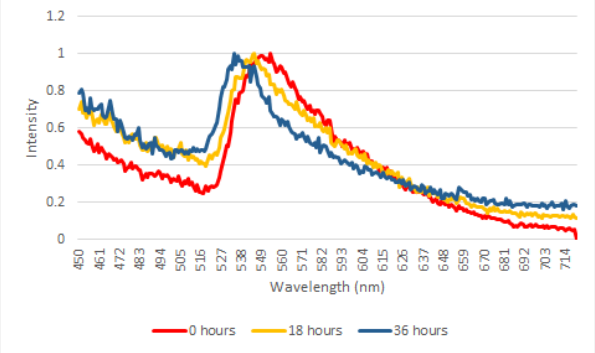

Figure 31: Normalized PL intensity spectra of the $TiO_2/MAPbBr_3$/spiro-OMeTAD triple layer sample with different aging times.

In summary, photoluminescence spectroscopy sheds light on a few key degradation processes of $MAPbBr_3$ samples. First, it corroborated what was observed about light degradation and light annealing effects in the absorption spectra. The light degradation effect leads to high defect density and quenches PL intensity by promoting nonradiative recombination; while light annealing effect improves crystallinity of perovskite thin film and decreases defect density and consequently enhances PL intensity by suppressing nonradiative decay. The interplay of the two

effects during aging are manifested in all the four samples by a fluctuation of PL intensity and changes of PL emission band width and PL peak positions. Second, PL spectroscopy provided insight into how ion accumulation at interfaces affects charge transfer processes in different samples. We observe that ion accumulation at TiO_2 (ETL) interface can partially block electron transfer from $MAPbBr_3$ to ETL, which is supported by the large PL enhancement observed in $MAPbBr_3/TiO_2$ double layer sample. However, the ion accumulation effect on charge transfer is much weaker in spiro-OMeTAD/$MAPbBr_3$ double layers and spiro-OMeTAD/$MAPbBr_3/TiO_2$ triple layers. Third, it elucidated that the light annealing can enhance charge transfer efficiency in the spiro-OMeTAD/$MAPbBr_3/TiO_2$ triple layers sample, providing a potential pathway to improve photovoltaic efficiency in perovskite solar cells.

Chapter 5: Conclusions

OMH perovskite samples, with TiO_2 and/or spiro-OMeTAD, of up to three layers were spin-coated onto thin glass substrates to study the degradation processes under a standard 1 sun illumination. These samples demonstrated the interfacial behavior of participant materials in perovskite solar cell chemistries. $MAPbI_3$ samples were images with UV-Vis spectroscopy. $MAPbBr_3$ samples were imaged with both UV-Vis and steady-state photoluminescence spectroscopy.

Interfacial chemistries have a direct impact on the stability of OMH perovskites in architectures that mimic those of PSCs. All samples demonstrated degradation after illumination. Across all samples, TiO_2 showed a marked acceleration of degradation. Spiro-OMeTAD also demonstrated degrading behavior, but with a less severe decrease in sample quality. Ion migration driven by illumination and ion accumulation at the ETL/HTL interfaces through specific interfacial chemistry drove this degradation. Furthermore, PL spectroscopy revealed defect density change inside the perovskite thin films and charge transfer efficiency change at perovskite/ETL and perovskite/HTL interfaces during degradation of the samples. However, it was observed that samples also benefited from light-based annealing and increases in crystallinity, which improves the stability of perovskites. The increased crystallinity of perovskite driven by light annealing was also observed to enhance interfacial charge transfer, providing a unique pathway to improve power conversion efficiency of perovskite solar cells.

Future work in this area may include the evaluation of additional HTL/ETL systems to optimize the longevity of PSCs. Another topic of interest arising from this research is unique three layer interfacial effects, investigating whether ions diffuse from the HTL to the ETL and whether that has any impact on stability. Other work could include investigating interfacial effects over an extended time frame.

Bibliography

1. Xu, Y.; Zhao, G.; Cai, Y. Preparation of Titanium by Electro-Deoxidation of CATIO3 in a Molten Cacl2-Nacl Salt. *International Journal of Electrochemical Science* **2021**, *16* (10), 211022. DOI:10.20964/2021.10.29.
2. Kojima, A.; Teshima, K.; Shirai, Y.; Miyasaka, T. Organometal Halide Perovskites as Visible-Light Sensitizers for Photovoltaic Cells. *Journal of the American Chemical Society* **2009**, *131* (17), 6050–6051. https://doi.org/10.1021/ja809598r.
3. Snaith, H. J. Perovskites: The Emergence of a New Era for Low-Cost, High-Efficiency Solar Cells. *The Journal of Physical Chemistry Letters* **2013**, *4* (21), 3623–3630. https://doi.org/10.1021/jz4020162.
4. Best Research-Cell Efficiency Chart. https://www2.nrel.gov/pv/cell-efficiency (accessed 2025-05-11).
5. Zheng, X.; Chen, B.; Yang, M.; Wu, C.; Orler, B.; Moore, R. B.; Zhu, K.; Priya, S. The Controlling Mechanism for Potential Loss in CH3Nh3PbBr3 Hybrid Solar Cells. *ACS Energy Letters* **2016**, *1* (2), 424–430. DOI:10.1021/acsenergylett.6b00215.
6. Stoumpos, C. C.; Malliakas, C. D.; Kanatzidis, M. G. Semiconducting Tin and Lead Iodide Perovskites with Organic Cations: Phase Transitions, High Mobilities, and Near-Infrared Photoluminescent Properties. *Inorganic Chemistry* **2013**, *52* (15), 9019–9038. https://doi.org/10.1021/ic401215x.
7. Perovskite Solar Cells. https://www.energy.gov/eere/solar/perovskite-solar-cells (accessed 2025-05-11).
8. Huang, X.; Taishi, T.; Wang, T.; Hoshikawa, K. Measurement of Temperature Gradient in Czochralski Silicon Crystal Growth. *Journal of Crystal Growth* **2001**, *229* (1–4), 6–10. DOI:10.1016/s0022-0248(01)01040-5.
9. WHO. *Guidelines for drinking-water quality: Fourth edition incorporating the first and second addenda*. World Health Organization. https://www.who.int/publications/i/item/9789240045064.
10. He, D.; Chen, P.; Steele, J. A.; Wang, Z.; Xu, H.; Zhang, M.; Ding, S.; Zhang, C.; Lin, T.; Kremer, F.; Xu, H.; Hao, M.; Wang, L. Homogeneous 2d/3D Heterostructured Tin

Halide Perovskite Photovoltaics. *Nature Nanotechnology* **2025**. DOI:10.1038/s41565-025-01905-4.

11. Miyasaka, T.; Kulkarni, A.; Kim, G. M.; Öz, S.; Jena, A. K. Perovskite Solar Cells: Can We Go Organic-free, Lead-free, and Dopant-free? *Advanced Energy Materials* **2019**, *10* (13). DOI:10.1002/aenm.201902500.

12. Schileo, G.; Grancini, G. Lead or No Lead? Availability, Toxicity, Sustainability and Environmental Impact of Lead-Free Perovskite Solar Cells. *Journal of Materials Chemistry C* **2021**, *9* (1), 67–76. DOI:10.1039/d0tc04552g.

13. Tumen-Ulzii, G.; Qin, C.; Matsushima, T.; Leyden, M. R.; Balijipalli, U.; Klotz, D.; Adachi, C. Understanding the Degradation of Spiro-ometad-based Perovskite Solar Cells at High Temperature. *Solar RRL* **2020**, *4* (10). DOI:10.1002/solr.202000305.
14. Krishna, B. G.; Ghosh, D. S.; Tiwari, S. Hole and Electron Transport Materials: A Review on Recent Progress in Organic Charge Transport Materials for Efficient, Stable, and Scalable Perovskite Solar Cells. *Chemistry of Inorganic Materials* **2023**, *1*, 100026. DOI:10.1016/j.cinorg.2023.100026.
15. Dong, Y.; Rombach, F. M.; Min, G.; Snaith, H. J.; Lin, C.-T.; Haque, S. A.; Macdonald, T. J. Dopant-Induced Interactions in Spiro-OMeTAD: Advancing Hole Transport for Perovskite Solar Cells. *Materials Science and Engineering: R: Reports* **2025**, *162*, 100875. https://doi.org/10.1016/j.mser.2024.100875.
16. Fatima, Q.; Ali Haidry, A.; Zhang, H.; El Jery, A.; Aldrdery, M. A Critical Review on Advancement and Challenges in Using TiO2 as Electron Transport Layer for Perovskite Solar Cell. *Materials Today Sustainability* **2024**, *27*. ttps://doi.org/10.1016/j.mtsust.2024.100857.
17. Chen, S.-H.; Ho, C.-M.; Chang, Y.-H.; Lee, K.-M.; Wu, M.-C. Efficient Perovskite Solar Cells with Low J-V Hysteretic Behavior Based on Mesoporous Sn-Doped Tio2 Electron Extraction Layer. *SSRN Electronic Journal* **2022**. DOI:10.2139/ssrn.4043391.
18. Meng, X.; Du, B.; Chen, X.; Li, Q.; Liu, J. Optimizating Tio2 Electron Transport Layer for MAPBBR3 Perovskite Solar Cells by Way of Ga Doping. *Journal of Alloys and Compounds* **2024**, *992*, 174647. DOI:10.1016/j.jallcom.2024.174647.
19. Raju, T. D.; Murugadoss, V.; Nirmal, K. A.; Dongale, T. D.; Kesavan, A. V.; Kim, T. G. Advancements in Perovskites for Solar Cell Commercialization: A Review. *Advanced Powder Materials* **2025**, *4* (2), 100275. DOI:10.1016/j.apmate.2025.100275.

20. McGovern, L.; Futscher, M. H.; Muscarella, L. A.; Ehrler, B. Understanding the Stability of $MAPbBr_3$ versus $MAPbI_3$: Suppression of Methylammonium Migration and Reduction

of Halide Migration. *The Journal of Physical Chemistry Letters* **2020**, *11* (17), 7127–7132. https://doi.org/10.1021/acs.jpclett.0c01822.

21. Sandhu, S.; Park, N.-G. Methodologies to Improve the Stability of High-Efficiency Perovskite Solar Cells. *Accounts of Materials Research* **2024**, *5* (12), 1544–1557. DOI:10.1021/accountsmr.4c00237.

22. Fei, C.; Li, B.; Zhang, R.; Fu, H.; Tian, J.; Cao, G. Highly Efficient and Stable Perovskite Solar Cells Based on Monolithically Grained CH3Nh3PBI3 Film. *Advanced Energy Materials* **2016**, *7* (9). DOI:10.1002/aenm.201602017.

23. Zheng, Y.; Ran, Y.; Xu, F.; Zhang, T.; Liu, Y.; Li, Y.; Li, X.; Li, G.; Aldamasy, M. H.; Yang, F.; Li, M. Stability Optimization for Perovskite Solar Cells with Two-dimensional Materials. *Solar RRL* **2024**, *8* (23). DOI:10.1002/solr.202400605.

24. Haryński, Ł.; Olejnik, A.; Grochowska, K.; Siuzdak, K. A Facile Method for Tauc Exponent and Corresponding Electronic Transitions Determination in Semiconductors Directly from UV–VIS Spectroscopy Data. *Optical Materials* **2022**, *127*, 112205. DOI:10.1016/j.optmat.2022.112205.

25. Photoluminescence Spectroscopy. https://www.ossila.com/pages/photoluminescence-spectroscopy (accessed 2025-05-11).

26. AG, F. Quantifying Trap States in Perovskite & Organic Solar Cells: Fluxim. https://www.fluxim.com/research-blogs/trap-states-perovskite-solar-cells (accessed 2025-05-11).

27. Tebyetekerwa, M.; Zhang, J.; Xu, Z.; Truong, T. N.; Yin, Z.; Lu, Y.; Ramakrishna, S.; Macdonald, D.; Nguyen, H. T. Mechanisms and Applications of Steady-State Photoluminescence Spectroscopy in Two-Dimensional Transition-Metal Dichalcogenides. *ACS Nano* **2020**, *14* (11), 14579–14604. DOI:10.1021/acsnano.0c08668.

28. Zhao, J.; Caselli, V. M.; Bus, M.; Boshuizen, B.; Savenije, T. J. How Deep Hole Traps Affect the Charge Dynamics and Collection in Bare and Bilayers of Methylammonium Lead Bromide. *ACS Applied Materials & Interfaces* **2021**, *13* (14), 16309–16316. DOI:10.1021/acsami.1c00714.

29. Mattiello, S.; Lucarelli, G.; Calascibetta, A.; Polastri, L.; Ghiglietti, E.; Podapangi, S. K.; Brown, T. M.; Sassi, M.; Beverina, L. Sustainable, Efficient, and Scalable Preparation of

Pure and Performing Spiro-OMeTAD for Perovskite Solar Cells. *ACS Sustainable Chemistry & Engineering* **2022**, *10* (14), 4750–4757.

30. Cao, Y.; Liu, Z.; Li, W.; Zhao, Z.; Xiao, Z.; Lei, B.; Zi, W.; Cheng, N.; Liu, J.; Tu, Y. Efficient and Stable MAPBI3 Perovskite Solar Cells Achieved via Chlorobenzene/Perylene Mixed Anti-Solvent. *Solar Energy* **2021**, *220*, 251–257. DOI:10.1016/j.solener.2021.03.055.
31. Eze, M. C.; Eze, H. U.; Ugwuanyi, G. N.; Alnajideen, M.; Atia, A.; Olisa, S. C.; Rocha, V. G.; Min, G. Improving the Efficiency and Stability of In-Air Fabricated Perovskite Solar Cells Using the Mixed Antisolvent of Methyl Acetate and Chloroform. *SSRN Electronic Journal* **2022**. DOI:10.2139/ssrn.4060807.

32. Basumatary, P.; Agarwal, P. Two-Step Fabrication of $$\hbox {mapbi}_{3}$$ Perovskite Thin Films with Improved Stability. *Bulletin of Materials Science* **2019**, *42* (6). DOI:10.1007/s12034-019-1959-1.
33. Tian, Y.; Scheblykin, I. G. Artifacts in Absorption Measurements of Organometal Halide Perovskite Materials: What Are the Real Spectra? *The Journal of Physical Chemistry Letters* **2015**, *6* (17), 3466–3470. DOI:10.1021/acs.jpclett.5b01406.

34. Chen, Y.; Wu, W.; Ma, R.; Wang, C. Perovskites Fabricated with Volatile Anti-Solvents for More Efficient Solar Cells. *Journal of Molecular Structure* **2019**, *1175*, 632–637. DOI:10.1016/j.molstruc.2018.08.021.

35. Nishimura, N.; Behera, R. K.; Katoh, R.; Kanda, H.; Murakami, T. N.; Matsuzaki, H. Unveiled Effects of the Methylammonium Chloride Additive on Formamidinium Lead Halide: Expediting Carrier Injection from the Photoabsorber to Carrier Transport Layers through Spontaneously Modulated Heterointerfaces in Perovskite Solar Cells. *Journal of Materials Chemistry C* **2024**, *12* (25), 9130–9138. DOI:10.1039/d4tc00843j.

36. Zhang, K.; Wang, Z.; Wang, G.; Wang, J.; Li, Y.; Qian, W.; Zheng, S.; Xiao, S.; Yang, S. A Prenucleation Strategy for Ambient Fabrication of Perovskite Solar Cells with High Device Performance Uniformity. *Nature Communications* **2020**, *11* (1). DOI:10.1038/s41467-020-14715-0.

37. Oh, J.; Lee, H.; Ryu, M.-Y. Effect of Antisolvent Application Time on Ch3nh3pbi3 Solar Cells in Ambient Atmosphere. *Current Applied Physics* **2023**, *56*, 119–125. DOI:10.1016/j.cap.2023.10.009.

38. Ge, C.; Xu, Q.; Liu, D.; Ye, W.; Zhu, Y.; Zhang, P.; Yang, J.; Liang, G.; Xu, L.; Zhou, Y.; Song, H.; Chen, C.; Tang, J. Light Radiation Annealing Enables Unidirectional

Crystallization of Vacuum-Assisted Sn–PB Perovskites for Efficient Tandem Solar Cells. *Energy & Environmental Science* **2025**, *18* (1), 430–438. DOI:10.1039/d4ee03419h.

39. Liu, D.; Wang, H.; Liao, F.; Di, H.; Li, H.; Zhao, J.; Zhao, X.; Song, J.; Lei, L.; Chen, C. Suppressing Ion Migration in Mapbi3 Polycrystalline Wafer with BMIMBF4 Ionic Liquid for X-ray Detection and Imaging. *Laser & Photonics Reviews* **2024**, *19* (2). DOI:10.1002/lpor.202401206.

40. Kim, T.; Park, S.; Iyer, V.; Shaheen, B.; Choudhry, U.; Jiang, Q.; Eichman, G.; Gnabasik, R.; Kelley, K.; Lawrie, B.; Zhu, K.; Liao, B. Mapping the Pathways of Photo-Induced Ion Migration in Organic-Inorganic Hybrid Halide Perovskites. *Nature Communications* **2023**, *14* (1). DOI:10.1038/s41467-023-37486-w.

41. Spiro-OMeTAD (Spiro-MeOTAD). https://www.ossila.com/products/spiro-ometad (accessed 2025-05-11).

42. Amiri, O.; Rezaee, A. E.; Teymourinia, H.; Salavati-Niasari, M.; Guo, L. J.; Baktash, A. New Strategy to Overcome the Instability That Could Speed up the Commercialization of Perovskite Solar Cells. *Advanced Materials Interfaces* **2019**, *6* (9). DOI:10.1002/admi.201900134.

43. Kim, S.; Bae, S.; Lee, S.-W.; Cho, K.; Lee, K. D.; Kim, H.; Park, S.; Kwon, G.; Ahn, S.-W.; Lee, H.-M.; Kang, Y.; Lee, H.-S.; Kim, D. Relationship between Ion Migration and Interfacial Degradation of CH3NH3PBI3 Perovskite Solar Cells under Thermal Conditions. *Scientific Reports* **2017**, *7* (1). DOI:10.1038/s41598-017-00866-6.

44. Jena, A. K.; Numata, Y.; Ikegami, M.; Miyasaka, T. Role of Spiro-Ometad in Performance Deterioration of Perovskite Solar Cells at High Temperature and Reuse of the Perovskite Films to Avoid PB-Waste. *Journal of Materials Chemistry A* **2018**, *6* (5), 2219–2230. DOI:10.1039/c7ta07674f.

45. Kasparavicius, E.; Franckevičius, M.; Malinauskiene, V.; Genevičius, K.; Getautis, V.; Malinauskas, T. Oxidized Spiro-Ometad: Investigation of Stability in Contact with Various Perovskite Compositions. *ACS Applied Energy Materials* **2021**, *4* (12), 13696–13705. DOI:10.1021/acsaem.1c02375.

46. Schuster, O.; Wientjes, P.; Shrestha, S.; Levchuk, I.; Sytnyk, M.; Matt, G. J.; Osvet, A.; Batentschuk, M.; Heiss, W.; Brabec, C. J.; Fauster, T.; Niesner, D. Looking beyond the Surface: The Band Gap of Bulk Methylammonium Lead Iodide. *Nano Letters* **2020**, *20* (5), 3090–3097. DOI:10.1021/acs.nanolett.9b05068.

47. Kim, M.; Yang, J. Characterization of Large-Energy-Bandgap Methylammonium Lead Tribromide (MAPBBR3) Perovskite Solar Cells. *Nanomaterials* **2023**, *13* (7), 1152. DOI:10.3390/nano13071152.

48. Wang, K.-H.; Li, L.-C.; Shellaiah, M.; Wen Sun, K. Structural and Photophysical Properties of Methylammonium Lead Tribromide (MAPBBR3) Single Crystals. *Scientific Reports* **2017**, *7* (1). DOI:10.1038/s41598-017-13571-1.

49. Zhang, Z.-Y.; Wang, H.-Y.; Zhang, Y.-X.; Hao, Y.-W.; Sun, C.; Zhang, Y.; Gao, B.-R.; Chen, Q.-D.; Sun, H.-B. The Role of Trap-Assisted Recombination in Luminescent Properties of Organometal Halide Ch3nh3pbbr3 Perovskite Films and Quantum Dots. *Scientific Reports* **2016**, *6* (1). DOI:10.1038/srep27286.

50. Miah, Md. H.; Rahman, Md. B.; Nur-E-Alam, M.; Islam, M. A.; Shahinuzzaman, M.; Rahman, Md. R.; Ullah, Md. H.; Khandaker, M. U. Key Degradation Mechanisms of Perovskite Solar Cells and Strategies for Enhanced Stability: Issues and Prospects. *RSC Advances* **2025**, *15* (1), 628–654. DOI:10.1039/d4ra07942f.

51. Tao, J.; Zhao, C.; Wang, Z.; Chen, Y.; Zang, L.; Yang, G.; Bai, Y.; Chu, J. Suppressing Non-Radiative Recombination for Efficient and Stable Perovskite Solar Cells. *Energy & Environmental Science* **2025**, *18* (2), 509–544. DOI:10.1039/d4ee02917h.

Figure Citations

1. Zhou, Y.; Herz, L. M.; Jen, A. K.-Y.; Saliba, M. Advances and Challenges in Understanding the Microscopic Structure–Property–Performance Relationship in Perovskite Solar Cells. *Nature Energy* **2022**, *7* (9), 794–807. DOI:10.1038/s41560-022-01096-5.
2. Morab, S.; Sundaram, M. M.; Pivrikas, A. Review on Charge Carrier Transport in Inorganic and Organic Semiconductors. *Coatings* **2023**, *13* (9), 1657. DOI:10.3390/coatings13091657.

3. Madadi, D.; Gharibshahian, I.; Orouji, A. A. High-Performance α-FAPBI3 Perovskite Solar Cells with an Optimized Interface Energy Band Alignment by a Zn(o,s) Electron Transport Layer. *Journal of Materials Science: Materials in Electronics* **2023**, *34* (1). DOI:10.1007/s10854-022-09565-z.